A spatial map of hepatic mitochondria uncovers functional heterogeneity shaped by nutrient-sensing signaling

Sun Woo Sophie Kang[1], Rory P. Cunningham[1], Colin B. Miller[1], Lauryn A. Brown[1], Constance M. Cultraro[1], Adam Harned[2,3], Kedar Narayan[2,3], Jonathan Hernandez[4], Lisa M. Jenkins[5], Alexei Lobanov[6], Maggie Cam[6], and Natalie Porat-Shliom[1,7]

1. Cell Biology and Imaging Section, Thoracic and GI Malignancies Branch, National Cancer Institute (NCI), National Institutes of Health (NIH), Bethesda, Maryland, USA.
2. Center for Molecular Microscopy, Center for Cancer Research, National Cancer Institute, National Institutes of Health, Bethesda, Maryland, USA.
3. Cancer Research Technology Program, Frederick National Laboratory for Cancer Research, Frederick, Maryland, USA.
4. Surgical Oncology Program, National Cancer Institute (NCI), National Institutes of Health (NIH), Bethesda, Maryland, USA.
5. Laboratory of Cell Biology, National Cancer Institute (NCI), National Institutes of Health (NIH), Bethesda, Maryland, USA.
6. CCR Collaborative Bioinformatics Resource (CCBR) National Cancer Institute (NCI), National Institutes of Health (NIH), Bethesda, Maryland, USA.
7. Correspondence: natalie.porat-shliom@nih.gov

Abstract

In the liver, mitochondria are exposed to different concentrations of nutrients due to their spatial positioning across the periportal (PP) and pericentral (PC) axis. How these mitochondria sense and integrate these signals to respond and maintain homeostasis is not known. Here, we combined intravital microscopy, spatial proteomics, and functional assessment to investigate mitochondrial heterogeneity in the context of liver zonation. We found that PP and PC mitochondria are morphologically and functionally distinct; beta-oxidation was elevated in PP regions, while lipid synthesis was predominant in the PC mitochondria. In addition, comparative phosphoproteomics revealed spatially distinct patterns of mitochondrial composition and

potential regulation via phosphorylation. Acute pharmacological modulation of nutrient sensing through AMPK and mTOR shifted mitochondrial phenotypes in the PP and PC regions, linking nutrient gradients across the lobule and mitochondrial heterogeneity. This study highlights the role of protein phosphorylation in mitochondrial structure, function, and overall homeostasis in hepatic metabolic zonation. These findings have important implications for liver physiology and disease.

Introduction

Mitochondria are highly dynamic organelles that play critical roles in cell physiology, including energy production through oxidative phosphorylation (OXPHOS), metabolic signaling pathways, and biosynthesis [1-5]. In response to changes in the environment, such as nutrient availability, mitochondria undergo remodeling through fission, fusion, and mitophagy [2,4]. These dynamic rearrangements in mitochondrial architecture are fundamental to mitochondrial function, morphology and homeostasis [4,5]. Further, these dynamic changes are modulated, in part, through post-translational modifications, like phosphorylation, allowing mitochondria to rapidly and reversibly adjust their metabolic output [6-8]. *In vivo*, mitochondria in cells within organs are exposed to varying levels of nutrients due to their spatial positioning with respect to the blood supply. How this affects and/or regulates mitochondrial dynamics is not known.

This is particularly important in the liver, a central metabolic organ that balances whole-body nutrient availability. Within the liver, hepatocytes are organized into polygonal units called lobules. Nutrient-rich blood flows unidirectionally into the lobule, entering through the hepatic artery and portal vein (which will hence be referred to as periportal; PP) and drains into a single central vein (pericentral; PC). Consequently, the hepatocytes are exposed to different levels of regional metabolites and metabolic burdens depending on their relative location within the lobule [9,10]. It has been previously shown that these gradients direct hepatocytes in different parts of the lobule to express different genes, a phenomenon known as liver zonation [10]. Wnt ligands secreted by PC endothelial cells are a major driver of zonal gene expression [11-13]. Although single-cell RNA sequencing has enhanced our understanding of liver zonation [14,15], the functional consequences are often inferred solely from gene expression.

39 Electron microscopy studies have revealed notable differences in mitochondrial
40 morphology between PP and PC hepatocytes [16-19]. These observations suggest that cells on the
41 PP-PC axis, separated by up to a mere 300 μm, possess mitochondria with distinct functions.
42 However, it is not known how spatial separation affects mitochondria functions *in vivo*.
43 Furthermore, whether mitochondrial variations are determined genetically or continuously
44 adjusted metabolically (via dynamic nutrient gradients) requires elucidation.

45 In the present study, we aimed to define the relationship between mitochondrial
46 function, structure, and spatial positioning in the hepatic lobule. We also sought to identify
47 mechanisms that regulate mitochondrial diversity during homeostasis. Our results highlight the
48 role of protein phosphorylation and nutrient sensing in dynamically tuning zonated
49 mitochondrial functions in the hepatic lobule. This is the first description of hepatic
50 mitochondrial zonation, combining structural and functional features that reveal distinct
51 subpopulations of mitochondria within the liver lobule.

52

53 **Results**

54 **A comparative mitochondrial proteome of spatially sorted hepatocytes**

55 To investigate how the spatial positioning of cells in the liver affects mitochondrial
56 functions, PP and PC hepatocytes from the livers of four ad-lib-fed mice were enriched using
57 unique surface markers and fluorescence-activated cell sorting (FACS; Fig 1A-C). E-cadherin and
58 CD73 antibodies were used to enrich PP and PC hepatocytes, respectively, and Western blots
59 were performed for validation (Fig 1D).

60 Next, PP and PC hepatocytes were subjected to tandem mass tag (TMT)-based
61 quantitative mass spectrometry for total proteome analysis. The goal was to gain insight into
62 mitochondrial functions by establishing a quantitative map of mitochondrial protein abundance
63 along the PP-PC axis. Principal component and hierarchical clustering analyses showed sample
64 grouping based on spatial origin (PP or PC) (Fig S1A-B). Of 5,018 proteins identified, 46% were
65 zonated, meaning they had a biased expression toward PP or PC hepatocytes (Fig. S1C-D; Sup
66 File 1). Pathway analysis highlighted PP and PC-restricted processes consistent with a previous
67 study describing gene expression [15] (Fig S1E-F).

68 The list of quantified proteins was compared with the murine MitoCarta 3.0 database,
69 which consists of 1,140 proteins. We identified 829 mitochondrial proteins, 422 of which were
70 enriched in PP mitochondria and 113 in PC mitochondria (Fig 2A and B). To gain insight into the
71 functions of PP and PC mitochondria, the top 25 unique proteins were selected, and their
72 location and pathway within the mitochondria were determined using MitoCarta 3.0 database
73 (Fig 2C and D). Selected mitochondrial proteins were also validated by immunofluorescence (Fig
74 S2).

75 Proteins enriched in PP mitochondria were primarily localized to the inner membrane or
76 the mitochondrial matrix and were involved in amino acid metabolism or OXPHOS. Thus, we
77 examined the spatial expression of selected OXPHOS proteins and found that PP mitochondria
78 expressed higher levels of nuclear and mitochondrial-encoded OXPHOS components (Fig. 2E). In
79 contrast, proteins enriched in PC mitochondria localized to the outer and inner mitochondrial
80 membranes and matrix. In addition to regulating mitochondrial structure, dynamics, and
81 contact with other organelles, many of the identified PC proteins are involved in lipid
82 metabolism, detoxification, and carbohydrate metabolism (Fig. 2D). Notably, citrate synthase
83 (CS), a tricarboxylic acid cycle (TCA cycle) enzyme, was highly expressed in PC mitochondria. In
84 addition to the TCA cycle, when transported into the cytosol, citrate can be a precursor for lipid
85 synthesis. Indeed, STRING analysis suggested a functional link between PC mitochondrial
86 proteins involved in pyruvate metabolism and phospholipid membrane biosynthesis and lipid
87 synthesis occurring in the cytosol (Fig 2F).

88 **Periportal mitochondria display enhanced bioenergetic capacity**

89 We next performed a functional evaluation of the PP and PC mitochondria to determine
90 their bioenergetic capacity. Intravital microscopy [20] was used to examine mitochondrial
91 membrane potential in the intact liver of anesthetized mice. Mitochondria were labeled with
92 MitoTracker green and TMRE, with the former labeling mitochondria matrix and the latter
93 indicating membrane potential. TMRE labeled mitochondria in PP regions more intensely,
94 indicating higher membrane potential (Fig 3A-B and Fig S3A-B). Isolated hepatocytes were
95 labeled with Anti-CD73, Anti-E-cadherin antibodies, and JC1, a ratiometric fluorescent reporter
96 of mitochondrial membrane potential. Consistent with the *in vivo* data, PP cells labeled in

97 suspension had higher mitochondrial membrane potential than PC cells (Fig 3C and D).
98 Together, these data show that PP mitochondria have a higher membrane potential that is not
99 disrupted by spatial sorting, allowing the use of these cells for further physiological evaluation.

100 Subsequently, mitochondrial oxygen consumption rate and substrate preferences were
101 evaluated using the Seahorse XF Analyzer in spatially sorted hepatocytes. PP hepatocytes
102 consumed up to double the amount of oxygen compared to PC cells (Fig 3E) and had higher
103 maximal respiration (Fig 3F). Next, substrate preference was determined by measuring the rate
104 of ATP production in the presence of inhibitors. The capacity of PP mitochondria to produce
105 ATP was significantly decreased by etomoxir, an irreversible inhibitor of fatty acid oxidation,
106 whereas, in PC mitochondria, UK 5099, an inhibitor of the mitochondrial pyruvate carrier that
107 inhibits pyruvate-dependent oxygen consumption, negatively impacted ATP production (Fig 3G
108 and H).

109 ATP levels in PP hepatocytes were significantly higher as measured by a luminescent
110 ATP Detection Kit (Fig 3I). On the other hand, citrate synthase expression and activity as well as
111 triglyceride (TG) levels were higher in PC hepatocytes (Fig 2D and Fig 3J-K). Likewise, lipid
112 droplets (LDs) which store TGs, were more abundant in PC regions of the lobule (Fig S4A).
113 Higher TG levels in PC cells could be the result of lower lipid oxidation, increased lipid uptake,
114 or decreased lipophagy. Alternatively, since high ATP levels inhibit citrate synthase activity [21,22],
115 the lower ATP levels in PC hepatocytes may permit citrate synthase activity and lipogenesis.

116 Consistent with a previous report [23], mRNA and protein abundance of the lipogenesis-
117 related enzymes Fasn (fatty acid synthase), Acly (ATP citrate synthase), Acaca (ACC1, acetyl-CoA
118 carboxylase), and Scd1 (Stearoyl CoA desaturase 1) displayed a PP bias or were unzonated (Fig
119 S4C-D). However, PP hepatocytes displayed higher levels of serine 79 phosphorylation, on
120 acetyl-CoA carboxylase (ACC1), which inhibits lipogenesis supporting the hypothesis that
121 lipogenesis preferentially occurs in PC hepatocytes (Fig S4B). This implies that the functional
122 specialization of hepatocytes is not only regulated by differential expression but also via
123 phosphorylation.

124 **Mitochondrial morphology and organization vary across the hepatic lobule**

125 To better understand the spatial organization of mitochondria in the hepatic lobule, we
126 used confocal microscopy to visualize mitochondria in liver sections from mito-Dendra2 mice [24].
127 Consistent with previous reports [16-19], an apparent dichotomy in mitochondrial architecture was
128 observed along the PP-PC axis, with short, round mitochondria in PP and tubulated
129 mitochondria in PC hepatocytes (Fig 4A and Movie S1 and S2). The transition between these
130 two phenotypes occurred in the mid-lobular area, with a limited number of cells containing
131 both phenotypes within a single cell (Fig 4A).
132 Mitochondrial topology was visualized in 3D and at nanometer resolution with Focused
133 Ion Beam Scanning Electron Microscopy (FIB-SEM) [25,26]. Initially, scanning electron microscopy
134 images of the hepatic lobule were used to identify PP and PC regions for FIB-SEM (Fig S5). Next,
135 FIB-SEM volumes of the selected cells were acquired, individual mitochondria segmented, and
136 mitochondrial volumentric models generated (Fig 4B-C and Movie S3 and S4; see Material and
137 Methods). Distinct subcellular organization of the mitochondrial network in different parts of
138 the lobule were apparent (Fig 4B and C). Mitochondria volume and surface area in PP cells were
139 approximately 2-fold greater than those measured in PC cells (Fig 4D and E). The sphericity
140 index also significantly differed between PP and PC, with mean values of 0.93 and 0.74,
141 respectively (Fig 4F). The higher mean values in PP hepatocytes indicate a shape closer to a
142 sphere as demonstrated by the round surfaces rendered (Fig 4C).
143 Larger mitochondrial volume in PP hepatocytes, together with higher bioenergetic
144 capacity (Fig 3) suggests that overall mitochondrial mass is higher in PP regions of the lobule.
145 Lending further support to this idea, mitochondrial DNA copy number, a commonly used
146 method to evaluate mitochondrial mass, was also higher in PP hepatocytes (Fig 4G).
147 Mitochondrial structural diversity, including the typical PP and PC morphologies described
148 above, was conserved in the human liver, suggesting a similar structure-function relationship
149 may apply (Fig S6). Taken together, mitochondrial structural variations across the lobule
150 strongly correlate with the functional diversity in lipid oxidation and biosynthesis under normal
151 physiological conditions.
152 **Enhanced mitophagy flux in PC hepatocytes**

153 Mitophagy, the selective degradation of mitochondria via autophagy, is stimulated in
154 response to various signals, including hypoxia, nutrient deprivation, and glucagon signaling [27,28].
155 In the liver, basal mitophagy is also activated by the daily feeding and fasting cycle [29,30]. To
156 evaluate if mitophagy is differentially regulated across the liver lobule, we applied intravital
157 microscopy of mitochondria-targeted Keima in ad-lib-fed mice (mtKeima) [31]. The mtKeima
158 protein has different excitation wavelengths depending on the acidity of the mitochondrial
159 environment; in a neutral environment, mtKeima excitation is at 440 nm, while in an acidic
160 environment, excitation is at 560 nm (Fig 5A). The ratio of acidic-to-neutral excitation is a
161 measure of mitophagy and the relative difference between mitophagy in the presence or
162 absence of the protease inhibitor leupeptin, is used to determine mitophagy flux. Tile scans of
163 entire lobules were acquired and ratios of acidic-to-neutral excitation were calculated in
164 selected regions (Fig 5B). While in saline-treated mice, mitophagy was consistently higher in PP
165 regions, leupeptin significantly increased mitophagy only in PC hepatocytes, suggesting a higher
166 mitophagy flux in PC regions. (Fig 5C). Notably, the increase in mtKeima fluorescence in PP
167 regions was driven by a higher signal in both the neutral and acidic compartments, while in PC
168 regions it was mainly due to an increase in the acidic compartments (compare grey scale insets
169 with and without leupeptin in Fig 5B). Similar trends were obtained with another mitophagy
170 reporter Cox8-EGFP-mCherry [32] (Fig S7A and B). The spatial differences in mtKeima fluorescence
171 intensities in PP and PC regions (Fig 5B) were not due to variations in mtKeima expression levels
172 (Fig S7C).
173 We further tested the spatial differences in mitophagy by evaluating the levels of the
174 mitophagy receptor Bnip3 and the autophagy marker LC3A/B using Western blots (Fig 5D). In
175 saline-treated mice, there were higher levels of Bnip3 in PC hepatocytes, and significantly
176 higher levels in mice treated with leupeptin, consistent with higher mitophagy flux in PC regions
177 (Fig 5D and E). On the other hand, the proportion of LC3A/B (an autophagy marker) was similar
178 in PP and PC hepatocytes, and leupeptin treatment had a comparable effect on both PP and PC
179 cells, suggesting uniform levels of basal autophagy across the lobule (Fig 5DF). Other
180 mitophagy-related proteins were enriched in PC hepatocytes (Fig S7D), as previously reported
181 [33,34]. Likewise, the lysosomal marker LAMP1 was distributed uniformly across the lobule, while

182 LAMP1-positive lysosomes containing mitochondria were more abundant in PC hepatocytes (Fig
183 S7E). Thus, basal mitophagy is higher in PC hepatocytes, which may be driven by the higher
184 expression of mitophagy-related proteins and contribute to the lower mitochondrial mass.

185 **Phosphoproteome highlights the role of nutrient sensing signaling in shaping mitochondrial**
186 **diversity**

187 Reversible protein phosphorylation has been linked to cellular and mitochondrial
188 metabolism [6-8,35,36]. To examine the role of phosphorylation in regulating mitochondrial spatial
189 heterogeneity and identify signaling pathways that may be involved, we profiled the
190 phosphoproteomes of PP and PC hepatocytes (Fig S8A-C). We identified 7,278 phosphopeptides
191 corresponding to 3686 phosphosites in 1,623 proteins (Fig 6A; Sup File 2). The majority of
192 phosphorylation sites were on serine residues (89%), with a smaller proportion identified on
193 threonine (10%) and tyrosine (1%) (Fig 6B). More than half of the proteins had a single
194 phosphorylation site (Fig 6C). Interestingly, the overall number of phosphosites with PP or PC
195 zonation was similar (Fig 6D), suggesting that ATP availability across the lobule (Fig 3A) is not
196 limiting in homeostasis.

197 Next, we performed a pathway analysis on zonated phospho-peptides to determine the
198 processes that may be influenced by phosphorylation (either activating or inhibiting) in each
199 hepatocyte population (Sup File 3). In PP hepatocytes, protein translation, metabolism, and
200 positive regulation of autophagy were most notably regulated via phosphorylation (Fig 6E). On
201 the other hand, multiple pathways related to lipid and phospholipid synthesis were represented
202 in PC cells (Fig 6F). Sequence analysis of phosphorylated peptides using the online tool Momo
203 (https://meme-suite.org/meme/tools/momo) revealed several phosphorylation motifs were
204 enriched in different parts of the lobule, suggesting potential involvement of distinct kinases
205 and signaling pathways (Sup File 4).

206 We also examined the phosphorylation of mitochondrial proteins, with mitochondrial
207 phosphoproteome shown in the volcano plot (Fig 6G) and the zonated phosphoproteins for
208 each hepatocyte group summarized in the table (Fig 6H and Sup File 5). Assessment of
209 upstream regulators/kinases using PhosphoSitePlus highlighted factors such as leptin, insulin,
210 mTOR, and AMPK as major drivers of the zonated phosphorylation (Sup File 6). To further

211 examine the role of nutrient sensing in shaping the zonated phosphoproteome, we surveyed all
212 zonated phosphopeptides for putative for AMPK and mTOR consensus sites using Group-based
213 Prediction System (GPS) 5.0. Approximately 50% of the PP or PC phosphorylation sites were
214 identified as putative AMPK or mTOR consensus sequences (Fig S8D). However, there was very
215 little overlap in AMPK or mTOR substrates within PP and PC cells (Fig S8E). This suggests that
216 although active throughout the lobule, AMPK and mTOR act on different substrates in PP and
217 PC hepatocytes. To further substantiate this, we examined the phosphorylation status of two
218 well-characterized mTOR substrates. Whereas phosphorylation on T389 of Ribosomal protein
219 S6 kinase (S6K) displayed a PC bias, phosphorylation on T37/T46 of Eukaryotic translation
220 initiation factor 4E (eIF4E)-binding protein 1 (4E-BP1), showed a PP bias, respectively (Fig S8F).
221 Together, these results highlight a potential role for nutrient-sensing signaling in shaping
222 zonated phosphoproteomes.

223 **Nutrient sensing signaling contributes to mitochondrial functional and structural**
224 **heterogeneity across the lobule**

225 Given the spatial variation in mitochondrial phospho-sites, their potential regulation by
226 the nutritional state, and the capacity of mitochondria to respond to nutrient fluctuations [1,8],
227 we hypothesized that nutrient-sensing signaling governs mitochondrial remodeling in
228 hepatocytes. To test this, and decouple protein phosphorylation from transcription, we
229 pharmacologically modulated AMPK or mTOR signaling *in vivo* and evaluated mitochondrial
230 membrane potential (JC1), and lipid content (BODIPY) via flow cytometry (Fig 7B and C). Drug
231 concentrations for acute response were determined by Western blotting of known downstream
232 effectors (Fig S9A and B). Activation of AMPK (AICAR) and the inhibition of mTOR (Torin) were
233 each associated with increased mitochondrial membrane potential in both PP and PC
234 hepatocytes (Fig 7B). The inhibition of AMPK (Compound C; Cpc) and activation of mTOR
235 (MHY1485) had no impact on membrane potential, suggesting the potential involvement of
236 other factors (Fig 7B). On the other hand, the inhibition of AMPK, significantly increased lipid
237 content in PC cells, and the activation of mTOR had a similar effect on PP cells, highlighting the
238 spatial coordination of these pathways in lipid homeostasis (Fig 7C). Notably, the drugs had an

239 acute effect on the mitochondria independent of cell size underscoring the complex spatial
240 regulation of nutrient-sensitive signaling in the intact liver (Fig S9C).

241 Finally, we performed microscopy studies in liver sections to examine if acute
242 modulation of AMPK or mTOR impacted mitochondrial morphology. PC mitochondria from
243 AICAR-treated mice had a round morphology with a higher sphericity index, similar to PP
244 mitochondria in vehicle-treated cells (Fig 7C and D). Conversely, mTOR activation induced
245 dense, elongated mitochondria in PP hepatocytes, with a lower sphericity index resembling the
246 phenotypes observed in PC hepatocytes (Fig 7C and D). Taken together, the results show that
247 mitochondrial zonation is acutely remodeled *in vivo* by nutrient-sensing signaling suggesting the
248 nutrient gradient fine-tune mitochondrial metabolic output.

249 Mitochondrial heterogeneity can be established through various mechanisms, including
250 differential gene expression (i.e. developmentally), dynamic gradients (i.e. metabolically), or a
251 combination. Correlation between Wnt-regulated genes and the mitochondrial proteomes of
252 both PP and PC were examined. We found a moderate negative correlation with the PP
253 mitochondrial proteome and a moderate positive correlation with the PC mitochondrial
254 proteome (Fig S9D). Overall, these experiments show that acute modulation of nutrient-sensing
255 pathways shifts mitochondrial functions to impact mitochondrial functional diversity. These
256 pathways work in concert with Wnt/β-catenin-regulated genes in determining the
257 mitochondrial proteomes of both PP and PC.

258

259 **Discussion**

260 In this study, we performed an in-depth characterization of mouse hepatic mitochondria
261 along the PP-PC axis and assessed the spatial heterogeneity of these mitochondria in two
262 populations of cells (Fig 1). We showed that mitochondria residing in hepatocytes adjacent to
263 the portal vein produce significantly higher levels of ATP through lipid oxidation and OXPHOS.
264 Roughly 300 μm apart, PC mitochondria oxidize pyruvate and produce higher citrate levels for
265 lipogenesis. This PP-PC dichotomy in mitochondrial function mirrors the spatial separation of
266 lipid utilization and biosynthesis in the liver. To our knowledge, this is the first spatial
267 assessment of the molecular makeup and functional specialization of hepatic mitochondria. It is

268 also the first in-depth investigation of how the physiological niche within the liver lobule alters
269 mitochondrial metabolism. This location-dependent functional heterogeneity highlights the
270 importance of considering mitochondrial disparity in understanding liver physiology and
271 disease.

272 Consistent with previous observations [16-19], we also found striking variations in
273 mitochondrial morphology across the PP-PC axis (Fig 4). Specifically, large spherical
274 mitochondria correlated with enhanced OXPHOS in PP hepatocytes (Fig 2E and 4A-F). This
275 morphology was previously shown to improve oxygen and nutrient exchange and tightly control
276 calcium concentrations, an essential regulator of OXPHOS and mitophagy [37,38]. Conversely,
277 longer, tubulated mitochondria (Fig 4A-F) may protect against mitochondrial degradation [37],
278 counterbalancing the higher mitophagy flux in PC regions (Fig 5A-C). Mitochondrial tubular
279 versus spherical morphology may also impact mitochondrial metabolic tasks; with tubular
280 mitochondria favoring enzymatic activities in the matrix, and spherical mitochondria improving
281 bioenergetic efficiency. Shirihai and colleagues recently demonstrated that mitochondrial
282 fragmentation, such as observed in PP hepatocytes, increases fatty acid oxidation [39]. We further
283 demonstrated a correlation between hepatic mitochondrial structure and function;
284 pharmacological modulation of major nutrient signaling pathways resulted in a remodeled
285 mitochondrial structure and its corresponding function (Fig 7).

286 Variations in mitochondrial fission and fusion are also likely to contribute to structural
287 diversity, as has been previously shown in other tissues [40,41]. We identified several candidates
288 that may be involved in fusion pathways by regulating mitochondrial dynamics and contact
289 sites in PC mitochondria (Fig 2D). On the other hand, mitochondrial morphology in PP
290 hepatocytes suggests that fission is favored. Mitochondrial fission can be mediated by the
291 phosphorylation of Mtfr1 or Mtfr1l, both of which showed a PP bias in our phosphoproteomic
292 analysis (Fig 6H). Indeed, phosphorylation of the same conserved site in human Mtfr1l by AMPK
293 was shown to cause mitochondrial fragmentation [42]. Further experiments are necessary to
294 examine the spatiotemporal regulation of mitochondrial fission-fusion dynamics Our finding
295 that mitochondrial morphology is conserved in the human liver (Fig S6), suggests that some
296 mechanisms are preserved across species and warrants further investigation.

297 Hepatic mitochondria not only display structural and functional heterogeneity, but they
298 also possess distinct phosphoproteomes associated with each mitochondrial population.
299 Despite higher ATP levels in PP hepatocytes (Fig 3I), the number of phosphosites was similar to
300 in PC (Fig 6D). This suggests unique cytosolic or mitochondrial kinases or phosphatases are
301 active in different cells. Indeed, we identified spatially distinct kinases reported to regulate the
302 mitochondrial phosphoproteome [6], including Prakaca (PKA catalytic subunit) in PP mitochondria
303 and, Pdha1 and Bckdk, in PC mitochondria (Fig 6H). Post-translational control of mitochondrial
304 metabolism through phosphorylation has been shown to be critical across mouse strains, age,
305 fasting/refeeding, and the onset of Type 2 diabetes [35]. Unexpectedly, the inhibitory
306 phosphorylation of Pdha1 was higher pericentrally (Fig 6H), which seemingly contradicts the
307 Seahorse data showing that PC hepatocytes rely on pyruvate for ATP production (Fig 3H).
308 However, the relative abundance of Pdha1 is also higher in PC hepatocytes (Sup File 1) which
309 could lead to overall higher levels of the active enzyme. Our study adds to this complexity by
310 demonstrating that differential regulation observed across the lobule is fundamental to hepatic
311 cellular homeostasis. While these phosphorylation sites were not characterized in this study,
312 combining the phosphoproteome data with functional studies allowed us to gain a system-level
313 perspective into the functional consequences of protein phosphorylation (Fig 6).
314 Our research indicates that protein phosphorylation, in conjugation with zonated
315 protein expression, plays a pivotal role in regulating various aspects of mitochondrial
316 functionality, quality control, and lipid handling in distinct hepatic zones. The primary
317 orchestrator of liver zonation at the transcriptional level is the Wnt/β-catenin signaling pathway
318 [12,13,43]. In agreement, we observed a correlation between the spatial distribution of
319 mitochondrial proteins and genes regulated by the Wnt pathway (Fig S9D). However, we also
320 found that mitochondrial proteins that display zonated phosphorylation, (Fig 6H), are intricately
321 linked with spatially controlled pathways, including lipogenesis (Fig 3 and Fig S4), mitophagy
322 (Fig 5 and Fig S7), and mitochondrial OXPHOS (Fig 3). Based on these observations, we
323 hypothesize that the establishment of liver zonation is not solely dictated by gene expression;
324 instead, it can be dynamically remodeled, through nutrient signaling pathways and protein
325 phosphorylation.

326 The regulation of mitophagy and lipogenesis through reversible phosphorylation is ideal.
327 It can be remodeled by nutrient-sensitive kinases (Fig 7), thus providing a quick mechanism for
328 mitochondria to adjust their metabolic output. Several phosphorylation sites on the mitophagy
329 receptor Bnip3 identified here are known to promote mitophagy [44-46]. We also demonstrate
330 functional zonation of lipogenesis through periportal inhibition of ACC1 (Fig S4B and 6H).
331 Although additional investigation into the complex spatial coordination of AMPK and mTOR is
332 required, our study shows that these kinases operate on distinct substrates in PP and PC cells
333 (Fig S8D-E), which has a direct impact on mitochondrial phenotypes. This is especially critical in
334 the liver, given its role in maintaining whole-body glucose homeostasis. We speculate that post-
335 translational modifications provide the flexibility required for these vital metabolic
336 adjustments, compared to the relatively sustained process of gene expression. Although further
337 experiments to test this hypothesis are needed, we predict that protein phosphorylation may
338 be the critical link between the observed discrepancies in function versus protein or gene
339 expression. This finding has significant implications beyond the liver for studies where function
340 is inferred from expression.

341 Advances in omics approaches and microscopy technologies have opened up new
342 avenues for research and discoveries in hepatic cell biology. Although liver zonation was
343 described nearly a century ago, we are only now starting to unravel how liver anatomy and the
344 gradient of factors within it affect liver function at the tissue level. Our study, for the first time,
345 demonstrates the delicate interplay between the function, shape, and space of hepatic
346 mitochondria. We reveal that protein phosphorylation is an additional regulatory layer, offering
347 spatial and temporal control of hepatic activities. Other post-translational modifications are
348 also likely at play. In the current study, due to the sample size required for phosphoproteome
349 and functional assays, we were limited to analyzing only two groups of hepatocytes. Therefore,
350 significant technological improvements are required to allow for further and deeper exploration
351 of liver zonation. Such advances are already underway with single-cell proteomics [47], allowing
352 increased spatial resolution in murine models and human samples. Ultimately, understanding
353 how the local physiological niche affects mitochondrial metabolism may be relevant for the
354 therapeutic modulation of these pathways in liver-related pathologies.

355

356 **Contact information**

357 Natalie Porat-Shliom, Center for Cancer Research, National Cancer Institute. Building 10, Room
358 12C207 MSC 1919, Bethesda, MD 20892. Phone: 240-760-6847. Email: natalie.porat-
359 shliom@nih.gov

360

361 **Financial Support**

362 This work was supported by the Intramural Research Program at the NIH, National Cancer
363 Institute (1ZIABC011828). This project has been funded in part with Federal funds from the
364 National Cancer Institute, National Institutes of Health, under Contract No. 75N91019D00024.
365 The content of this publication does not necessarily reflect the views or policies of the
366 Department of Health and Human Services, nor does mention of trade names, commercial
367 products, or organizations imply endorsement by the U.S. Government. The authors have no
368 conflicts to report.

369

370 **Acknowledgments**

371 We thank Dr. Wen-Xing Ding for the Cox8-EGFP-mCherry-AAV8 construct. Drs. Torn Finkel and
372 Nuo Sun for Mt-Keima mice . We thank Drs. Sudipto Das and Thorkell Andresson from the CCR
373 proteomics Facility at the Frederick National Laboratory for Cancer Research and members of
374 the NCI LGI Flow Cytometry Core. We thank Aayush Bhatawadekar and Abhishek Bhardwaj for
375 volume renderings and morphological calculations based on vEM mitochondrial segmentation.
376 Dr. Daniel Feliciano acquired images in Figures 4A and S2A. We thank Pranali Pathare Mangat of
377 3P Scientific Communications for providing scientific editing support. We are grateful for the
378 critical comments made by members of the Porat-Shliom lab.

379

380 **References**

381 1 Picard, M. & Shirihai, O. S. Mitochondrial signal transduction. *Cell Metab* **34**, 1620-1653
382 (2022). https://doi.org:10.1016/j.cmet.2022.10.008
383 2 Glancy, B. Visualizing Mitochondrial Form and Function within the Cell. *Trends Mol Med*
384 **26**, 58-70 (2020). https://doi.org:10.1016/j.molmed.2019.09.009

385 3 Hoppins, S. The regulation of mitochondrial dynamics. *Curr Opin Cell Biol* **29**, 46-52
386 (2014). https://doi.org:10.1016/j.ceb.2014.03.005
387 4 Friedman, J. R. & Nunnari, J. Mitochondrial form and function. *Nature* **505**, 335-343
388 (2014). https://doi.org:10.1038/nature12985
389 5 Westermann, B. Bioenergetic role of mitochondrial fusion and fission. *Biochim Biophys*
390 *Acta* **1817**, 1833-1838 (2012). https://doi.org:10.1016/j.bbabio.2012.02.033
391 6 Niemi, N. M. & Pagliarini, D. J. The extensive and functionally uncharacterized
392 mitochondrial phosphoproteome. *Journal of Biological Chemistry* **297** (2021).
393 https://doi.org:ARTN 100880
394 10.1016/j.jbc.2021.100880
395 7 Kolitsida, P., Zhou, J. W., Rackiewicz, M., Nolic, V., Dengjel, J. & Abeliovich, H.
396 Phosphorylation of mitochondrial matrix proteins regulates their selective mitophagic
397 degradation (vol 116, pg 20517, 2019). *P Natl Acad Sci USA* **116**, 24374-24374 (2019).
398 https://doi.org:10.1073/pnas.1918594116
399 8 Grimsrud, P. A. *et al.* A quantitative map of the liver mitochondrial phosphoproteome
400 reveals posttranslational control of ketogenesis. *Cell Metab* **16**, 672-683 (2012).
401 https://doi.org:10.1016/j.cmet.2012.10.004
402 9 Jungermann, K. in *Regulation of Hepatic Metabolism: Intra- and Intercellular*
403 *Compartmentation* (eds Ronald G. Thurman, Frederick C. Kauffman, & Kurt
404 Jungermann) 445-469 (Springer US, 1986).
405 10 Cunningham RP, P.-S. N. Liver Zonation – Revisiting Old Questions With New
406 Technologies. *Front. Physiol.* (2021). https://doi.org:10.3389
407 11 Soto-Gutierrez, A., Gough, A., Vernetti, L. A., Taylor, D. L. & Monga, S. P. Pre-clinical and
408 clinical investigations of metabolic zonation in liver diseases: The potential of
409 microphysiology systems. *Exp Biol Med (Maywood)* **242**, 1605-1616 (2017).
410 https://doi.org:10.1177/1535370217707731
411 12 Sekine, S., Lan, B. Y., Bedolli, M., Feng, S. & Hebrok, M. Liver-specific loss of beta-catenin
412 blocks glutamine synthesis pathway activity and cytochrome p450 expression in mice.
413 *Hepatology* **43**, 817-825 (2006). https://doi.org:10.1002/hep.21131
414 13 Benhamouche, S. *et al.* Apc tumor suppressor gene is the "zonation-keeper" of mouse
415 liver. *Dev Cell* **10**, 759-770 (2006). https://doi.org:10.1016/j.devcel.2006.03.015
416 14 Brosch, M. *et al.* Epigenomic map of human liver reveals principles of zonated
417 morphogenic and metabolic control. *Nat Commun* **9**, 4150 (2018).
418 https://doi.org:10.1038/s41467-018-06611-5
419 15 Halpern, K. B. *et al.* Single-cell spatial reconstruction reveals global division of labour in
420 the mammalian liver. *Nature* **542**, 352-356 (2017). https://doi.org:10.1038/nature21065
421 16 Novikoff, A. B. Cell heterogeneity within the hepatic lobule of the rat: staining reactions.
422 *J Histochem Cytochem* **7**, 240-244 (1959). https://doi.org:10.1177/7.4.240
423 17 Deane, H. W. A cytological study of the diurnal cycle of the liver of the mouse in relation
424 to storage and secretion. *Anat Rec* **88**, 39-65 (1944). https://doi.org:DOI
425 10.1002/ar.1090880104
426 18 JM, K. Comparative and experimental studies on the cytology of the liver. (1933).
427 19 Smith, D. M. THE ONTOGENETIC HISTORY OF THE MITO- CHONDRIA OF THE HEPATIC
428 CELL OF THE WHITE RAT. (1931).

429 20 Weigert, R., Porat-Shliom, N. & Amornphimoltham, P. Imaging cell biology in live
430 animals: ready for prime time. *J Cell Biol* **201**, 969-979 (2013).
431 https://doi.org:10.1083/jcb.201212130
432 21 Fang, M. & Lowenstein, J. M. Citrate and the conversion of carbohydrate into fat. The
433 regulation of fatty acid synthesis by rat liver extracts. *Biochem J* **105**, 803-811 (1967).
434 https://doi.org:10.1042/bj1050803
435 22 Shepherd, D. & Garland, P. B. The kinetic properties of citrate synthase from rat liver
436 mitochondria. *Biochem J* **114**, 597-610 (1969). https://doi.org:10.1042/bj1140597
437 23 Massalha, H. *et al.* A single cell atlas of the human liver tumor microenvironment. *Mol*
438 *Syst Biol* **16** (2020). https://doi.org:ARTN e9682
439 10.15252/msb.20209682
440 24 Pham, A. H., McCaffery, J. M. & Chan, D. C. Mouse lines with photo-activatable
441 mitochondria to study mitochondrial dynamics. *Genesis* **50**, 833-843 (2012).
442 https://doi.org:10.1002/dvg.22050
443 25 Conrad, R. & Narayan, K. Instance segmentation of mitochondria in electron microscopy
444 images with a generalist deep learning model trained on a diverse dataset. *Cell Syst* **14**,
445 58-71 e55 (2023). https://doi.org:10.1016/j.cels.2022.12.006
446 26 Collinson, L. M. *et al.* Volume EM: a quiet revolution takes shape. *Nat Methods* **20**, 777-
447 782 (2023). https://doi.org:10.1038/s41592-023-01861-8
448 27 Macleod, K. F. Mitophagy and Mitochondrial Dysfunction in Cancer. *Annu Rev Canc Biol*
449 **4**, 41-60 (2020). https://doi.org:10.1146/annurev-cancerbio-030419-033405
450 28 Palikaras, K., Lionaki, E. & Tavernarakis, N. Mechanisms of mitophagy in cellular
451 homeostasis, physiology and pathology. *Nat Cell Biol* **20**, 1013-1022 (2018).
452 https://doi.org:10.1038/s41556-018-0176-2
453 29 Manella, G. & Asher, G. The Circadian Nature of Mitochondrial Biology. *Front Endocrinol*
454 *(Lausanne)* **7**, 162 (2016). https://doi.org:10.3389/fendo.2016.00162
455 30 Jacobi, D. *et al.* Hepatic Bmal1 Regulates Rhythmic Mitochondrial Dynamics and
456 Promotes Metabolic Fitness. *Cell Metab* **22**, 709-720 (2015).
457 https://doi.org:10.1016/j.cmet.2015.08.006
458 31 Sun, N. *et al.* Measuring In Vivo Mitophagy. *Mol Cell* **60**, 685-696 (2015).
459 https://doi.org:10.1016/j.molcel.2015.10.009
460 32 Ma, X. & Ding, W. X. A fluorescence imaging based-assay to monitor mitophagy in
461 cultured hepatocytes and mouse liver. *Liver Res* **5**, 16-20 (2021).
462 https://doi.org:10.1016/j.livres.2020.12.002
463 33 Droin, C. *et al.* Space-time logic of liver gene expression at sub-lobular scale. *Nat Metab*
464 (2021). https://doi.org:10.1038/s42255-020-00323-1
465 34 Springer, M. Z. *et al.* BNIP3-dependent mitophagy promotes cytosolic localization of
466 LC3B and metabolic homeostasis in the liver. *Autophagy* **17**, 3530-3546 (2021).
467 https://doi.org:10.1080/15548627.2021.1877469
468 35 Niemi, N. M. *et al.* Pptc7 is an essential phosphatase for promoting mammalian
469 mitochondrial metabolism and biogenesis. *Nature Communications* **10** (2019).
470 https://doi.org:ARTN 3197
471 10.1038/s41467-019-11047-6

36 Ardito, F., Giuliani, M., Perrone, D., Troiano, G. & Lo Muzio, L. The crucial role of protein phosphorylation in cell signaling and its use as targeted therapy. *International Journal of Molecular Medicine* **40**, 271-280 (2017). https://doi.org:10.3892/ijmm.2017.3036

37 Rambold, A. S., Kostelecky, B., Elia, N. & Lippincott-Schwartz, J. Tubular network formation protects mitochondria from autophagosomal degradation during nutrient starvation. *Proceedings of the National Academy of Sciences* **108**, 10190-10195 (2011). https://doi.org:doi:10.1073/pnas.1107402108

38 Han, S., Zhang, M., Jeong, Y. Y., Margolis, D. J. & Cai, Q. The role of mitophagy in the regulation of mitochondrial energetic status in neurons. *Autophagy* **17**, 4182-4201 (2021). https://doi.org:10.1080/15548627.2021.1907167

39 Ngo, J. *et al.* Mitochondrial morphology controls fatty acid utilization by changing CPT1 sensitivity to malonyl-CoA. *Embo J*, e111901 (2023). https://doi.org:10.15252/embj.2022111901

40 Benador, I. Y. *et al.* Mitochondria Bound to Lipid Droplets Have Unique Bioenergetics, Composition, and Dynamics that Support Lipid Droplet Expansion. *Cell Metabolism* **27**, 869-+ (2018). https://doi.org:10.1016/j.cmet.2018.03.003

41 Porat-Shliom, N., Harding, O. J., Malec, L., Narayan, K. & Weigert, R. Mitochondrial Populations Exhibit Differential Dynamic Responses to Increased Energy Demand during Exocytosis In Vivo. *iScience* **11**, 440-449 (2019). https://doi.org:10.1016/j.isci.2018.12.036

42 Tilokani, L. *et al.* AMPK-dependent phosphorylation of MTFR1L regulates mitochondrial morphology. *Sci Adv* **8**, eabo7956 (2022). https://doi.org:10.1126/sciadv.abo7956

43 Russell, J. O. & Monga, S. P. Wnt/beta-Catenin Signaling in Liver Development, Homeostasis, and Pathobiology. *Annu Rev Pathol* **13**, 351-378 (2018). https://doi.org:10.1146/annurev-pathol-020117-044010

44 He, Y. L. *et al.* BNIP3 phosphorylation by JNK1/2 promotes mitophagy via enhancing its stability under hypoxia. *Cell Death Dis* **13**, 966 (2022). https://doi.org:10.1038/s41419-022-05418-z

45 Poole, L. P., Bock-Hughes, A., Berardi, D. E. & Macleod, K. F. ULK1 promotes mitophagy via phosphorylation and stabilization of BNIP3. *Sci Rep* **11**, 20526 (2021). https://doi.org:10.1038/s41598-021-00170-4

46 Cho, Y. K. *et al.* STK3/STK4 signalling in adipocytes regulates mitophagy and energy expenditure. *Nat Metab* **3**, 428-441 (2021). https://doi.org:10.1038/s42255-021-00362-2

47 Rosenberger, F. A. *et al.* Spatial single-cell mass spectrometry defines zonation of the hepatocyte proteome. *bioRxiv*, 2022.2012.2003.518957 (2022). https://doi.org:10.1101/2022.12.03.518957

48 Stefkovich, M. L., Kang, S. W. S. & Porat-Shliom, N. Intravital Microscopy for the Study of Hepatic Glucose Uptake. *Curr Protoc* **1**, e139 (2021). https://doi.org:10.1002/cpz1.139

49 Ben-Moshe, S. *et al.* Spatial sorting enables comprehensive characterization of liver zonation. *Nat Metab* **1**, 899-911 (2019). https://doi.org:10.1038/s42255-019-0109-9

50 Gougelet, A. *et al.* T-cell factor 4 and β-catenin chromatin occupancies pattern zonal liver metabolism in mice. *Hepatology* **59**, 2344-2357 (2014). https://doi.org:https://doi.org/10.1002/hep.26924

516 51 Quiros, P. M., Goyal, A., Jha, P. & Auwerx, J. Analysis of mtDNA/nDNA Ratio in Mice.
517 *Current Protocols in Mouse Biology* **7**, 47-54 (2017).
518 https://doi.org:https://doi.org/10.1002/cpmo.21
519 52 Baena, V. *et al.* FIB-SEM as a Volume Electron Microscopy Approach to Study Cellular
520 Architectures in SARS-CoV-2 and Other Viral Infections: A Practical Primer for a
521 Virologist. *Viruses* **13**, 611 (2021).
522 53 Conrad, R. & Narayan, K. Instance segmentation of mitochondria in electron microscopy
523 images with a generalist deep learning model trained on a diverse dataset. *Cell Systems*
524 **14**, 58-71.e55 (2023). https://doi.org:https://doi.org/10.1016/j.cels.2022.12.006
525

526

527 **Figure Legends**

528

529 **Figure 1. Spatial enrichment of PP and PC hepatocytes. (A)** Schematic diagram depicting the
530 workflow. Hepatocytes were isolated from the murine liver using two-step collagenase
531 perfusion, after which unique surface markers were applied to label cells. Labeled cells were
532 then enriched using fluorescence-activated cell sorting (FACS) to obtain hepatocytes from
533 different zones. **(B)** Immunofluorescence staining of a liver section showing the zonal
534 distribution of CD73 (cyan) and E-cadherin (magenta). **(C)** Two-dimensional scatter plot of
535 hepatocytes labeled with CD73 and E-cadherin. **(D)** Western blot of spatially sorted
536 hepatocytes. Abbreviations: Periportal (PP), pericentral (PC), glutamine synthetase (GS).

537

538 **Figure 2. Comparative mitochondrial proteome of spatially sorted hepatocytes. (A)** Total
539 number of non-mitochondrial proteins (grey) and mitochondrial proteins (green) was detected
540 by mass spectrometry (left). Percentage of periportal (PP), pericentral (PC), and unzonated (UZ)
541 mitochondrial proteins (right); zonated expression based on a p-value (0.05). **(B)** Volcano plot
542 shows the $\log_2$ PC/PP fold-change (x-axis) and the $-\log_{10}$ p-value (y-axis) for mitochondrial
543 proteins. **(C-D)** Spatial distribution of the top 25 PP or PC mitochondrial proteins. Proteins were
544 color-coded to reflect their cellular function. Pathways were listed based on the frequency at
545 which they appeared. **(E)** Abundance of representative mitochondrial respiratory chain
546 proteins, both nuclear and mitochondria encoded, are shown with box and whisker plots. **(F)**
547 Bioinformatic STRING analysis of the PC mitochondria proteomic data. The interaction map

548 illustrates the functional association of PC mitochondrial metabolism with cytosolic lipid
549 synthesis. Data presented as mean ± SD. *p < 0.05, **p < 0.01, ***p < 0.001, ****p < 0.0001.
550
551 **Figure 3. PP mitochondria display higher bioenergetic capacity. (A)** Intravital microscopy of the
552 hepatic lobule labeled with tetramethylrhodamine ethyl ester (TMRE), and MitoTracker Green
553 to evaluate the relative mitochondrial membrane potential. The scale bar is 100 μm. **(B)**
554 Mitochondrial membrane potential was evaluated by measuring fluorescence intensity (AU)
555 along a PP-PC axis line. **(C-D)** Measurement of mitochondrial membrane potential using JC-1
556 and flow cytometry in spatially sorted hepatocytes. Dot plots of a representative experiment is
557 shown. The bar graph shows three independent experiments. **(E)** Oxygen consumption rate
558 (OCR) in spatially sorted hepatocytes using the XF Mito Stress Test Kit and Seahorse XF96
559 Analyzer. Samples were normalized to cell number. **(F)** Maximum respiration capacity in
560 spatially sorted hepatocytes expressed relative to PP. The bar graph shows four independent
561 experiments. **(G-H)** Substrate dependency assay in spatially sorted hepatocytes using the
562 MitoFuel Flex test. ATP production rate relative to PP is shown in cells treated with etomoxir,
563 UK5099, or BPTES. The bar graph shows the results of four independent experiments. **(I)** ATP
564 content relative to PP in spatially sorted hepatocytes using the colorimetric luciferase assay
565 from three independent experiments. **(J)** Citrate synthase activity relative to PP in spatially
566 sorted hepatocytes from 5 independent experiments. **(K)** Intracellular triglyceride (TG)
567 concentration relative to PP in spatially sorted hepatocytes from 3 independent experiments.
568 Data presented as mean ± SD; ns, *p < 0.05, **p < 0.01, ***p <0.001.
569
570 **Figure 4. Mitochondrial morphology and organization across the lobule. (A)** Confocal image of
571 the PP-PC axis in liver sections from Mito-Dendra2 transgenic mice. Mitochondria are shown in
572 white, and actin was labeled with phalloidin in red. Enlarged insets of a representative PP (left)
573 and PC (right) cell are shown. **(B)** Mitochondria were visualized by Focused Ion Beam Scanning
574 Electron Microscopy (FIB-SEM). Representative sections of PP (left) and PC (right) cells. Nucleus
575 (N), Lipid droplet (LD). **(C)** Segmentation and volume rendering of mitochondria from PP (left)
576 and PC (right) cells using Mito-Net and empanada-napari. **(D-F)** Quantification of mitochondrial

577 morphological features including volume, surface area, and sphericity index (a measure of
578 similarity to a perfect sphere (=1)). A collection of 175 mitochondria in PP and 250 in PC were
579 analyzed. **(G)** Quantification of relative mtDNA copy number by qPCR in spatially sorted
580 hepatocytes. The bar graph shows four independent experiments. Data presented as
581 mean±SD. ** $p < 0.01$, ****$p < 0.0001$.
582
583 **Figure 5. PC mitochondria display higher turnover via mitophagy. (A)** mtKeima is a pH-
584 sensitive mitophagy reporter. The ratio between the 440 nm (green; neutral pH) and 560 nm
585 (red; acidic pH) excitation measures the proportion of mitochondria undergoing mitophagy. **(B)**
586 Intravital microscopy of transgenic mice expressing mtKeima in saline-injected or leupeptin-
587 injected mice. Representative images of the hepatic lobule and magnified insets of PP and PC
588 regions **(C)** Quantification of mitophagy in PP and PC regions expressed as a fold change relative
589 to PP cells. Bar graph shows four independent experiments. **(D)** Immunoblots of Bnip3 and
590 LC3A/B of unsorted (total) and sorted PP and PC hepatocyte populations from livers treated
591 with either saline or leupeptin. Mouse 1 (M1); Mouse 2 (M2) **(E-F)** Quantification of Bnip3
592 expression and LC3B/A ratio. Bar graphs show six independent experiments. Data presented as
593 mean±SD. ns, *$p < 0.05$, **$p < 0.01$, ***$p < 0.001$.
594
595 **Figure 6. Phosphoproteome highlights spatially regulated pathways contributing to**
596 **mitochondrial phenotypes. (A)** Overview of phosphopeptides, phosphosites, and
597 phosphoproteins identified in the phosphoproteome. **(B)** Proportion of phosphorylated serine
598 (p-S), threonine (p-T), and tyrosine (p-Y) residues in the identified phosphopeptides. **(C)**
599 Proportion of proteins identified with a certain number of phosphorylated residues per protein.
600 **(D)** Number of phosphosites with a PP, PC, or unzonated (UZ) bias is shown in the bar graph. **(E-**
601 **F)** The PP or PC zonated phosphoproteins were analyzed using GO enrichment analysis. **(G)**
602 Mitochondrial phosphoproteome is shown in a volcano plot with $\log_2$ PC/PP fold-change (*x-axis*)
603 and the $-\log_{10}$ p-value (y-axis). **(H)** Selected zonated mitochondrial phosphoproteins are shown
604 in the table, including the phosphosites and the cellular function of the protein. Dash and

605 comma marks distinguish between potential and identified sites, respectively. Activating
606 phosphosites (green); Inhibitory (purple); uncharacterized (black).
607
608 **Figure 7. Nutrient sensing signaling contributes to mitochondrial functional and**
609 **morphological diversity. (A and B)** AMPK or mTOR signaling was modulated *in vivo* by injecting
610 an activating drug, AICAR or MHY1485, or an inhibitory drug Cpc or Torin, respectively. The
611 impact on mitochondrial membrane potential (JC-1) and lipid droplets (BODIPY) was evaluated
612 using flow cytometry. Bar graphs show 3-5 independent experiments. **(C)** Confocal images of
613 hepatocytes from liver sections of Mito-Dendra2 mice treated with vehicle, AICAR, or
614 MHY1485. Mitochondria are shown in white, and phalloidin outlines hepatocytes in red. Scale
615 bar= 3um. **(D)** Mitochondrial sphericity in mice treated with vehicle, AICAR, or MHY1485 was
616 quantified. Data are presented as mean. ns, *$p < 0.05$, **$p < 0.01$, ***$p < 0.001$, ****$p <$
617 0.0001.
618
619 **Figure S1. Comparative proteomics of spatially sorted hepatocytes. (A)** Principal component
620 analysis (PCA) and frequency histogram of spatially sorted hepatocytes analyzed with mass
621 spectrometry. **(B)** Correlation Matrix Heatmap of proteomics data. **(C)** Pie chart depicting the
622 percentage of PP, PC, and UZ proteins based on p-value (0.05). **(D)** Volcano plot showing the *PC*
623 to PP $\log_2$ fold-change (x-axis) and the $-\log_{10}$ p-value (y-axis) for identified proteins. **(E and F)** GO
624 enrichment analysis of the proteomics data in the spatially sorted cell.
625
626 **Figure S2. Immunofluorescence of representative PP and PC mitochondrial proteins.**
627 **(A)** Confocal image of the liver lobule from Mito-Dendra2 mice (green) stained with E-cadherin
628 to label PP regions (yellow) and Aldh1b1, a PP mitochondrial protein (magenta). Magnified
629 insets show the overlay of E-cadherin and Aldh1b1 only. Scale bar: 15 µm. **(B)** Confocal image of
630 the liver lobule from Mito-Dendra2 mice (green) stained with E-cadherin to label PP regions
631 (yellow) and Oat, a PC mitochondrial protein (magenta). Magnified insets show the overlay of E-
632 cadherin and Oat only. Scale bar: 15 µm.
633

634 **Figure S3: E-cadherin-positive hepatocytes display higher membrane potential. (A-B)** Intravital
635 microscopy of the hepatic lobule in Mito-Dendra2 mouse labeled with TMRE (red), and E-
636 cadherin (white). **(A)** Low magnification of the hepatic lobule. Scale bar: 30 μm. **(B)** Close up on
637 the PP-PC axis. Scale bar: 20 μm.
638
639 **Figure S4. Lipid synthesis is pericentral in the murine liver. (A)** Confocal image of a liver section
640 labeled with Lipidtox (lipid droplets; red) and phalloidin (actin; cyan), showing the non-uniform
641 distribution of lipid droplets across the PP-PC axis. **(B)** Representative immunoblot and
642 quantification of acetyl-CoA carboxylase 1 (ACC1, Acaca) relative phosphorylation (S79) in
643 spatially sorted hepatocytes. Bar graph shows five independent experiments. **(C)** RNA levels of
644 key lipogenesis enzymes in spatially sorted hepatocytes. Bar graph shows three independent
645 experiments. **(D)** Protein abundance of key lipogenesis enzymes identified by proteomics. Data
646 presented as mean ± SD. ns, **p <0.05, **p < 0.01, ***p < 0.001.
647
648 **Figure S5.** Scanning Electron Microscopy (SEM) of the lobule highlighting regions of interest
649 selected for FIB-SEM. SEM of the PP-PC axis in a liver section was performed to mark PP and PC
650 regions for FIB-SEM. Insets show PP and PC hepatocytes where striking variations in
651 mitochondrial morphology are observed.
652
653 **Figure S6. Mitochondrial morphologies are conserved in the human liver.** Confocal image of
654 fixed human liver sections labeled with phalloidin (actin; yellow) and TOM20 (outer
655 mitochondrial membrane; green). Scale bar: 50μm. Insets of representative PP and PC
656 hepatocytes show distinct morphological features (arrows). Scale bar: 5μm.
657
658 **Figure S7. PC mitochondria display higher mitophagy flux. (A)** Confocal microscopy of liver
659 sections from mice transduced with Cox8-EGFP-mCherry adenovirus. Representative PP and PC
660 cells are shown from saline or leupeptin-treated mice. Scale bar: 5μm. **(B)** The Cox8-EGFP-
661 mCherry reporter was used to measure mitophagy by calculating the percent of the
662 mitophagosome area normalized to the whole cell area in saline or leupeptin-treated mice. Bar

663 graph shows 15-20 cells quantified from 3 mice. **(C)** Keima protein expression in hepatocytes
664 isolated from one wild-type mouse and two mtKeima mice (M1 and M2). Sorted (PP and PC)
665 and total are shown for mtKeima only. **(D)** The abundance of mitophagy-related proteins
666 identified by proteomics is shown in box and whisker plots. Mitochondrial fission regulator 1
667 (Mtfr1); Bcl2 interacting protein 3 (Bnip3); GABA type A receptor-associated protein-like 2
668 (Gabarapl2); GABA type A receptor-associated protein like (Gabarapl). **(E)** Confocal images of PP
669 and PC hepatocytes from Mito-Dendra2 mice (green), treated with saline or leupeptin and
670 stained with the lysosomal marker LAMP1 (magenta) and actin (yellow). Arrowheads point to
671 mitochondria (green) inside lysosomes (magenta). Data presented as mean±SD. ns, *p < 0.05,
672 **p<0.01, ***p<0.001***p < 0.001.
673
674 **Figure S8. Comparative phosphoproteome in spatially sorted hepatocytes. (A)** Principal
675 component analysis (PCA) and **(B)** Correlation Matrix Heatmap of the phosphoproteome data
676 set. **(C)** Volcano plot showing the $\log_2$ *PC/*PP fold-change (x-axis) and the -$\log_{10}$ p-value (y-axis).
677 **(D)** Group-based Prediction System (GPS 5.0) was used to predict mTOR and AMPK
678 phosphorylation sequences. **(E)** Complete list of mTOR and AMPK substrates identified in PP
679 and PC. **(E)** Representative immunoblot and quantification of mTOR substrates pS6K (T389) and
680 p4E-BP (T37/46) in spatially sorted hepatocytes. Bar graphs show five to six independent
681 experiments. Data presented as mean±SD. ns, *p < 0.05.
682
683 **Figure S9. Nutrient sensing signaling regulates mitochondrial heterogeneity. (A)**
684 Determination of AICAR and Compound C (CpC) concentrations for *in vivo* modulation of AMPK
685 signaling. Drug efficacy was evaluated by Western blotting for pACC1 (S79) levels. **(B)**
686 Determination of MHY1485 and Torin concentrations for *in vivo* modulation of mTOR signaling.
687 Drug efficacy was evaluated by Western blotting for p4EBP1(Thr37/Thr46) levels. **(C)** Mice
688 were treated with two doses of vehicle, AMPK inhibitor (Compound C) or activator (AICAR), or
689 mTOR inhibitor (Torin I) or activator (MHY1485). Graphs show the evaluation of drug effect on
690 cell size measured by flow cytometry from three to five independent experiments. **(D)**

691 Correlation plot of Wnt-activated genes and PP or PC mitochondrial proteome. Data presented
692 as mean ± SD. ns, *p < 0.05, **p < 0.01, ***p < 0.001, ****p < 0.0001.
693
694 **Movie S1.** Confocal z-stack of PP mitochondria
695 **Movie S2.** Confocal z-stack of PC mitochondria
696 **Movie S3.** FIB-SEM and volume rendering of PP mitochondria
697 **Movie S4.** FIB-SEM and volume rendering of PC mitochondria
698
699 **Supplementary files 1-3 and 6 will become available when the manuscript is accepted for**
700 **publication**
701
702 **Supplementary File 4:** Modification Motifs (MoMo) analysis
703
704 **Supplementary File 5:** Extended table of mitochondrial phosphoproteins
705
706 **Material and methods**
707
708 **Animal experiments**
709 Experiments were approved by the Institutional Animal Care and Use Committee of the
710 National Cancer Institute and comply with the Guide for the Care and Use of Laboratory
711 Animals (National Institutes of Health publication 86-23, revised 1985). All experiments were
712 conducted on ad libitum-fed, eight-to-ten-week-old male mice; C57BL/6J (strain# 000664),
713 Mito-Dendra2 (strain# 018397) [24] obtained from Jackson Laboratories and the mtKeima line
714 were a gift from Dr. Toren Finkel [31].
715
716 **Intra-cardiac fixation, tissue processing, and immunofluorescence**
717 Mice were anesthetized with 250 mg/kg Xylazine, and 50 mg/kg Ketamine (diluted in saline)
718 injected intraperitoneally (i.p.). The liver was fixed by transcardial perfusion of ice-cold PBS for
719 2 min followed by ice-cold 4% paraformaldehyde (PFA) in PBS at a rate of 5 ml/min. Livers were
720 harvested and stored in 4% PFA in PBS overnight and processed in a sucrose gradient before
721 embedding in OCT (Tissue-Tek). Blocks were kept at -80 °C until 10 µm thick slices were made
722 with a cryostat and slides prepared. Slides were stored at -80 °C until thawed, rehydrated, and

723 blocked with 0.1% Triton X-100 and 10% FBS in PBS for 1 h at room temperature. Next, slides
724 were incubated with primary antibody at 4 °C overnight. The following day, slides were washed
725 three times, 15 min each, then incubated with a secondary antibody for 1 h at room
726 temperature. After three 15-min washes, slides were mounted with Fluoromount-G and a
727 coverslip (#1).
728
729 **Confocal microscopy and image processing**
730 Tile scans and z stacks were acquired using a Leica SP8 inverted confocal laser scanning
731 microscope using a 63x oil objective and a 1.4 numerical aperture. Images were deconvolved
732 using the LIGHTNING module in LAS X.
733
734 **Human tissue collection for immunofluorescence and imaging**
735 Human tissue was obtained under an NIH IRB-approved protocol (13-C-0076) for risk-reducing
736 surgery performed on patients with germline genetic mutation(s). All tissues procured, which
737 included liver samples used in this study, were grossly normal as determined by the surgeon
738 and histopathologically normal as determined by a board-certified pathologist. Of note, all
739 tissue was obtained within 20 min of incision. Tissues were fixed overnight in 4% PFA in PBS
740 overnight and processed in a sucrose gradient before embedding in OCT (Tissue-Tek).
741
742 **Measurement of mitochondrial membrane potential via intravital microscopy**
743 Intravital microscopy was performed as previously described [48]. Mitotracker Green FM (250
744 µM) and tetramethylrhodamine ethyl ester (TMRE, 200 µM) were consecutively injected retro-
745 orbitally to label mitochondria with/without mitochondrial membrane potential in livers of
746 C57BL/6J. After 30 min of incubation per dye, the liver was exposed to the microscope stage
747 with the mouse under anesthesia, and images were acquired using excitation at 480 nm and
748 532 nm. The fluorescence intensity of TMRE and Mitotracker Green FM was analyzed across the
749 PP-PC axis through line scanning with ImageJ. Additionally, Alexa Fluor® 647 anti-mouse/human
750 CD324 (E-cadherin, 0.5 µg/g) was retro-orbitally injected to label PP regions in the liver of Mito-
751 Dendra2 mice. Mito-Dendra2 mice were used instead of using Mitotracker Green FM dye to

752 observe all mitochondria despite mitochondrial membrane potential and only TMRE (200 μM)
753 was retro-orbitally injected and incubated for 30 min before imaging. Images were acquired
754 using excitation at 480 nm, 532 nm, and 647 nm.

755 **Measurements of mitophagy**

756 Mitophagy was measured in mtKeima mice [31] or C57BL/6J mice injected with Ad-Cox8-EGFP-
757 mCherry ($1x10^9$ PFU diluted in 200 μl of PBS) [32] using intravital microscopy as previously
758 described [48]. Lysosome inhibitor leupeptin (80 mg/kg), or saline was injected i.p. 16 h prior to
759 the experiment. A second dose of leupeptin (40 mg/kg) or saline was administered 12 h later.
760 Three to five mice were analyzed per experiment. This leupeptin treatment protocol was used
761 prior to isolating and sorting cells into PP and PC populations for immunoblot analysis of
762 mitophagy proteins.

763

764 **Western blot**

765 Proteins from primary hepatocytes or whole liver were extracted by homogenization in RIPA
766 lysis buffer (150 mM NaCl, 0.1% Triton X-100, 0.5% sodium deoxycholate, 0.1% sodium dodecyl
767 sulfate, and 50 mM Tris HCl pH 8.0) containing EDTA, PMSF, and Halt Inhibitor Cocktail (Thermo
768 Fisher), followed by centrifugation at 13,000 rpm at 4 °C for 30 min. Protein concentration was
769 determined using a Pierce™ BCA Protein Assay Kit (Thermo Fisher). Lysates were heated at
770 95 °C for 5 min, and 5-10 μg aliquots fractionated by SDS-PAGE then transferred to
771 nitrocellulose (0.45 μm) membrane (Bio-Rad). Membranes were blocked for 1 h at room
772 temperature in 5% BSA in 1x Tris-buffered saline + 0.1% Tween 20 (TBST), then incubated with
773 primary antibody diluted in 5% BSA in TBST at 4 °C overnight. Membranes were washed three
774 times with TBST then incubated in secondary antibody 1 h at room temperature. Membranes
775 were washed three times with TBST, then Clarity ECL western blot substrate solution (Bio-Rad)
776 was applied for detection and imaged using the ChemiDoc Imaging System (Bio-Rad). Bands
777 were quantified with ImageJ.

778

779 **Liver Perfusion and hepatocyte isolation**

780 Livers of anesthetized mice were perfused by inserting a 22-gauge syringe into the portal vein
781 and delivering 25 ml of pre-warmed (37 °C) perfusion buffer [Krebs-Henseleit buffer (Sigma)
782 with 0.5 µM EDTA], followed by 25 ml collagenase A buffer [Krebs-Henseleit buffer, with 0.1
783 mM Ca_2Cl and 0.4 mg/ml collagenase A (Sigma)]. After perfusion, livers were transferred to a
784 Petri dish, flooded with cold PBS, and hepatocytes were gently released using forceps.
785 Dissociated cells were collected and filtered through a 100 µm cell strainer. Cells were
786 centrifuged at 100 G for 5 min at 4 °C to obtain hepatocyte-enriched cells. Pellets were
787 resuspended in cold PBS, filtered through a 40 µm cell strainer, and centrifuged at 100 G for 5
788 min at 4 °C. Percoll diluted in 10x Hank's buffer (Sigma) was added to the cell suspension and
789 centrifuged at 100 G for 5 min at 4 °C. The supernatant containing dead cells was removed by
790 aspiration. The pellet was resuspended in cold PBS, and cell number and viability were
791 determined.

792 **Fluorescence-activated cell sorting (FACS) of PP and PC populations**

793 Cell sorting was performed on a FACSAria Fusion cell sorter (BD Biosciences). Forward and side
794 light scatter was used to distinguish cells from debris and to identify single cells. Zombie-Green
795 fixable live dead dye (1:500, BioLegend) was used to discriminate between live and dead cells.
796 PP and PC populations were identified using anti-E-cadherin-PE and anti-CD73-APC antibody
797 staining (1:150; BioLegend). PP- and PC-specific gates were set after spectral compensation
798 using appropriate fluorescent minus (FMO) controls. The protocol was developed based on [49].
799 To sort PP and PC hepatocyte populations from mtKeima mice, BD OptiBuild™ BUV395 Rat Anti-
800 Mouse CD324/E-Cadherin (1:125, BD Bioscience) was used to stain PP hepatocyte populations.
801 For E-cadherin negative populations (PC), FSC-A and SSC-A plot was used to further exclude
802 smaller sized hepatocytes as PC hepatocytes (CD73 positive) was generally found to be bigger in
803 cell size than PP hepatocytes.
804

805 **Protein Digestion and TMT labeling**

806 Cells were lysed in 50 mM HEPES, pH 8.0, 8 M urea, and 10% methanol, followed by sonication.
807 Lysates were clarified by centrifugation, and protein concentration quantified using a BCA
808 protein estimation kit (Thermo Fisher). A 250 ug aliquot was alkylated and digested by

809 incubating overnight at 37 °C in trypsin at a ratio of 1:50 (Promega). Digestion was acidified by
810 adding formic acid (FA) to a final concentration of 1% and desalted using Pierce peptide
811 desalting columns according to the manufacturer's protocol. Peptides were eluted from the
812 column using 50% ACN/0.1% FA, dried in a speed vac and kept frozen at -20 °C for further
813 analysis.
814 For TMT labeling, 125 ug of each sample was reconstituted in 50 µl of 50 mM HEPES, pH 8.0,
815 500 ug of TMTpro-16plex label (Thermo Fisher) in 100% ACN. After incubating the mixture for 1
816 h at room temperature with occasional mixing, the reaction was terminated by adding 8 µl of
817 5% hydroxylamine. As there were more than 16 samples, we generated a pooled sample
818 consisting of equal amounts of lysate from each condition and TMT labeled. The pool was
819 added to each TMT experiment. The TMT-labeled peptides were pooled and dried in a speed
820 vac. The samples were desalted, and excess TMT labels were removed using peptide desalting
821 columns (Thermo Fisher). A 100 ug aliquot of labeled peptide mixture was fractionated using
822 high pH reversed-phase, and the remaining peptide mixture was used for phospho-enrichment.
823
824 **Phosphopeptide enrichment**
825 Phosphopeptides were enriched from the TMT-labeled peptides using the SMOAC (Sequential
826 enrichment of Metal Oxide Affinity Chromatography) method. First, the phosphopeptides were
827 enriched using the HiSelect TiO_2 phosphopeptide enrichment kit (Thermo Fisher) according to
828 the manufacturer's protocol. The flow-through and wash from the TiO_2 enrichment kit were
829 then combined and enriched using the HiSelect Fe-NTA phosphopeptide enrichment kit
830 (Thermo Fisher). The enriched phosphopeptides obtained by both methods were dried by
831 speed vac and stored at -20 °C until analysis by mass spectrometry.
832
833 **High pH reversed-phase fractionation**
834 The first-dimensional separation of peptides was performed using a Waters Acquity UPLC
835 system coupled with a fluorescence detector (Waters) using a 150 mm x 3.0 mm Xbridge
836 Peptide BEM™ 2.5 µm C18 column (Waters) operating at 0.35 ml/min. The dried peptides were
837 reconstituted in 100 µl of mobile phase A solvent (3 mM ammonium bicarbonate, pH 8.0).

838 Mobile phase B was 100% acetonitrile (Thermo Fisher). The column was washed with mobile
839 phase A for 10 min followed by gradient elution 0-50% B (10-60 min) and 50-75% B (60-70 min).
840 Fractions were collected every minute. These 60 fractions were pooled into 24 fractions.
841 Fractions were vacuum centrifuged, and lyophilized fractions were stored at -80°C until analysis
842 by mass spectrometry.
843
844 **Mass Spectrometry acquisition**
845 The lyophilized peptide fractions were reconstituted in 0.1% TFA and subjected to nanoflow
846 liquid chromatography (Thermo Ultimate^{TM} 3000RSLC nano LC system, Thermo Fisher) coupled
847 to an Orbitrap Eclipse mass spectrometer (Thermo Fisher). Peptides were separated using a low
848 pH gradient and 5-50% ACN over 120 min in a mobile phase containing 0.1% formic acid at a
849 300 nl/min flow rate. MS scans were performed in the Orbitrap analyzer at a resolution of
850 120,000 with an ion accumulation target set at 4e^{5} and max IT set at 50 ms over a mass range of
851 400-1600 m/z. Ions with a determined charge state between 2 and 5 were selected for MS2
852 scans in the ion trap with CID fragmentation (Turbo; NCE 35%; maximum injection time 35 ms;
853 AGC 1 × 10^{4}). The spectra were searched using the Real Time Search Node in the tune file
854 using mouse Uniprot database using Comet search algorithm with TMT16 plex (304.2071 Da)
855 set as a static modification of lysine and the N-termini of the peptide. Carbamidomethylation of
856 cysteine residues (+57.0214 Da) was set as a static modification, while oxidation of methionine
857 residues (+15.9949 Da) was set up as a dynamic modification. For the selected peptide, an
858 SPS–MS3 scan was performed using up to 10 *b*- and *y*-type fragment ions as precursors in an
859 Orbitrap at 50,000 resolution with a normalized AGC set at 500 followed by maximum injection
860 time set as "Auto" with a normalized collision energy setting of 65.
861
862 The enriched phospho-samples were reconstituted in 0.1% TFA and analyzed using an Orbitrap
863 Eclipse mass spectrometer. Peptides were separated using a low pH gradient, and FAIMS was
864 enabled during data acquisition with the compensation voltages set at -45V, -60V, and -75V set
865 up at the first run, -50V, -65V, and -80V for the second run and -55V, -70V and -85V for the last
866 run. MS scans were performed in the Orbitrap analyzer at a resolution of 120,000 with an ion

867 accumulation target set at $4e^5$ and max IT set at 50ms over a mass range of 350-1600 m/z. Ions
868 with a known charge state between 2 and 6 were selected for MS2 scans. A cycle time of 1 sec
869 was used for each CV, and a quadrupole isolation window of 0.4 m/z was used for MS/MS
870 analysis. An Orbitrap at 15,000 resolution with a normalized AGC set at 250 followed by
871 maximum injection time set as "Auto" with a normalized collision energy setting of 38 was used
872 for MS/MS analysis. The node "Turbo TMT" was switched on for the high-resolution acquisition
873 of TMT reporter ions.
874
875 **Data Analysis**
876 Acquired MS/MS spectra were searched against the mouse Uniprot protein database and a
877 contaminant protein database using SEQUEST in the Proteome Discoverer 2.4 software
878 (Thermo Fisher). The precursor ion tolerance was set at 10 ppm, and the fragment ions
879 tolerance was set at 0.02 Da, with methionine oxidation included as a dynamic modification.
880 For the phospho-enriched samples, serine, threonine, and tyrosine phosphorylation were set as
881 variable modifications. Carbamidomethylation of cysteine residues and TMTpro16 plex
882 (304.2071 Da) was set as static modification of lysine and the N-terminus of the peptide.
883 Trypsin was specified as the proteolytic enzyme, with up to 2 missed cleavage sites allowed.
884 Searches used a reverse sequence decoy strategy to control for the false peptide discovery, and
885 identifications were validated using the Percolator algorithm in Proteome Discoverer 2.4.
886
887 Reporter ion intensities were adjusted to correct for lot-specific impurities according to the
888 manufacturer specification, and the abundances of the proteins were quantified using the
889 summation of the reporter ions for all identified peptides. A two-step normalization procedure
890 was applied to a 24-plex TMT experiment [2 TMT experiments with 12 samples each]. First, the
891 reporter abundances were normalized across all the channels to account for equal peptide
892 loading. Secondly, the intensity from the pooled sample was used to normalize the batch effect
893 from the multiple TMT experiments. Samples were further normalized using the Voom
894 algorithms and quantile normalization from the Limma R package (v3.40.6). We evaluated the
895 significance of a given protein, phosphopeptide, or normalized phosphopeptide change using

896 Limma, where zonation was determined by the p-value (0.05) and/or FC (≥1.2). Pathway
897 enrichment analysis was performed using Fisher's Exact test with GO database. MitoCarta 3.0
898 was used to classify of the identified proteins and phosphoproteins into mitochondrial and non-
899 mitochondrial proteins. GraphPad Prism 9 and BioRender were used for visualization.
900
901 **Prediction of mTOR and AMPK activity using Group-based Prediction System (GPS)**
902 All peptides with PP or PC zonation were extrapolated as 15 AA sequence with the phosphosite
903 in the center. Peptides without a specific site were excluded. Duplicate sequences were
904 removed, and sequences were analyzed using GPS 5.0 (AMPK and mTOR selected) at medium
905 threshold. The sequences analyzed and the output from GPS are listed in Supplementary File 6.
906

907 **MoMo motif analysis**

908 Motif analyses of PP or PC phosphopeptides were performed using the web tool available
909 at: https://meme-suite.org/meme/tools/momo, v5.5.4. All identified 15 AA sequences without
910 duplicates for each PP and PC quantified phosphosite were analyzed with a p-value threshold at
911 10^{-6}. The results from this analysis are listed in Supplementary File 4.

912

913 **WNT-activated genes correlation**

914 We examined identified mitochondrial proteins associated with WNT signaling transduction[50].
915 PP and PC were separately analyzed by computing the $\log_2$ ratio of the mean protein
916 abundance over the geomean from the raw data. These values were then used to examine
917 Spearman correlation value with log2 ratio of the mean gene expression levels from WNT-
918 hyperactivating liver-specific APC knockout and control mouse liver samples.

919

920 **Seahorse assay**

921 A Seahorse XFe96 Analyzer and XF Mito Stress Test Kit (Agilent Technologies) were used to
922 measure the oxygen consumption rate (OCR) and extracellular acidification rate (ECAR) of PP
923 and PC-sorted cells. A day before the assay, the cartridge sensor was hydrated overnight with
924 Seahorse Bioscience Calibration Solution at 37 °C without CO_2. After sorting, cells were seeded
925 at 5.0×10^4 cells/well, in a 96-well seahorse plate and allowed to adhere for 2 h. After 2 h,
926 media was replaced with serum-free Seahorse XF Base media containing glucose, pyruvate, and
927 glutamine (pH 7.4), and cells were incubated at 37 ˚C in a non-CO_2 incubator for 1 h. OCR and
928 ECAR were measured after the injection of oligomycin (1.5 μM), FCCP (1 μM), and
929 rotenone/antimycin (0.5 μM). The XF Mito Stress Test Kit was used together with an XF Mito
930 Fuel kit to test fuel dependency. Three inhibitors, UK5099 (2 μM), BPTES (3 μM), and etomoxir
931 (4 μM), were added to measure the dependency of cells on the three primary mitochondrial
932 fuels to produce ATP; glucose, glutamine, and long-chain fatty acids, respectively. Average
933 protein amount of PP and PC seeded wells were examined with BCA for normalization. To
934 overcome reading variations within each population, and measure the effect of the inhibitors,
935 the measurements of the wells treated with inhibitors were further normalized to the first basal

936 reading of the group treated with the vehicle (control). Measurements for ATP production rate
937 and maximum respiration capacity were presented as a percent normalized to PP. Bar graph
938 shows data from four independent experiments presented as mean±SD. Each independent
939 experiment was conducted with five to twelve replicates per population and treatment.
940
941 **ATP measurement assay**
942 The bioluminescence ATP assay kit was used according to manufacturer instructions
943 (Invitrogen) to analyze spatially sorted hepatocytes. ATP levels were calculated and normalized
944 according to protein amount.
945
946 **Citrate Synthase activity assay**
947 Citrate Synthase (CS) activity was analyzed following the manufacturer protocol (Abcam). After
948 collecting the cells via FACS, cells were lysed. A 50 µl aliquot of supernatant or standard GSH
949 solution with 50 µl of reaction buffer was added per well in a 96-well plate to measure the
950 absorbance (OD 412 nm) in kinetic mode at 25 °C for 40 min. CS activity was calculated based
951 on two different time points considering the dilution factor and cell number, then normalized
952 to the PP fraction.
953
954 **Triglyceride (TG) measurement assay**
955 After cell isolation and FACS, the sorted PP and PC cells were pelleted, washed twice with cold
956 PBS, and lysed on ice for 30 min. Lysates were centrifuged at 13,000 rpm for 10 min at 4 °C and
957 the supernatant collected. A TG-colorimetric GPO-PAP assay kit (Elab Science) was used to
958 determine TG content, following manufacturer instructions. TG levels were calculated
959 according to protein amount and normalized to PP fraction.
960
961 **DNA and RNA isolation**
962 RNA was isolated from spatially sorted cells using the RNeasy mini kit and QIAshredder
963 homogenizer columns (Qiagen). Total DNA was isolated using the DNeasy Blood and Tissue kit
964 (Qiagen).

965

966 **Quantitative PCR**

967 A High-Capacity RNA to cDNA kit (Thermo Fisher) was used to synthesize random-primed cDNA
968 from 600 ng DNAse treated RNA. Real-time PCR was conducted in 384 well-plates using a ViiA7
969 Real-time PCR system (Applied Biosystems). Singleplex reactions (10 µl) containing a FAM-MGB
970 expression assay for the gene of interest (Acaca Mm01304289_m1, Acly Mm01302282_m1,
971 Fasn Mm00662319_m1, Scd1 Mm00772290_m1) or endogenous control (Ppia
972 Mm02342430_g1) (Thermo Fisher) were performed using cDNA synthesized from 3 ng RNA and
973 1x Fast Advanced Master Mix (Thermo-without Amp Erase UNG). The comparative Ct method
974 (delta, delta Ct) was used to determine relative expression normalized to Ppia (Applied
975 Biosystems® ViiA™ 7Real-Time PCR System Getting Started Guides).

976

977 **mtDNA copy number determination**

978 Mitochondrial DNA content was measured by comparing the DNA copy number of two
979 mitochondrial encoded genes (ND1 and 16S rRNA) to HK, a nuclear-encoded gene[51]. The
980 mitochondrial to nuclear DNA ratio (mtDNA/nDNA) was determined by Real-time PCR using an
981 ABI Viia7 Real-Time PCR System (Applied Biosystems). Because mitochondrial genes lack
982 introns, it was possible to use TaqMan gene expression assays for mtDNA copy number.
983 Singleplex reactions (10 µl) containing FAM-MGB assays for ND1 Mm04225274_s1, Rnr2
984 Mm04260181_s1, or HK2 Mm00193901_cn (Applied Biosystems) were performed in
985 quadruplicate using 384 well plates with 10 ng DNA and 1x Universal Master Mix (Applied
986 Biosystems-without Amp Erase UNG). Determination of mtDNA content was performed using
987 the comparative Ct method (delta, delta Ct) with normalization to HK2 as an internal reference
988 (Applied Biosystems® ViiA™ 7Real-Time PCR System Getting Started Guides).

989

990 **Drug treatment and flow cytometry assay**

991 Mice were treated with two doses of either vehicle, Compound C (CpC, 20 mg/kg), 5-
992 Aminoimidazole-4-carboxamide ribonucleotide (AICAR, 0.5 mg/kg), Torin I (20 mg/kg) or
993 MHY1485 (20 mg/kg) before primary hepatocytes were isolated via perfusion. Hepatocytes

994 were then labeled with Cy-PE/PE-anti-E-cadherin and APC-anti-CD73 and either JC1 (5 μM) or
995 BODIPY-493/503 (2 μM) for 20 min at 37 °C. The fluorescent signal was measured by BD
996 LSRFortessa (BD Biosciences) cell analyzer. Consistent with FACS, forward and side light scatter
997 was used to distinguish cells from debris and to identify single cells.
998
999 **Sample prep and imaging for FIB-SEM**
1000 The structured sample preparation protocol based on the sample preparation widget from
1001 EMPIAR (https://www.ebi.ac.uk/empiar/widget) can be accessed at: 10.5281/zenodo.8422314.
1002 Briefly, lower left lobes dissected from normally fed mouse livers were fixed in Karnovsky's
1003 fixative for 2 h at room temperature, rinsed (all rinses were typically five times 3 min each at
1004 room temperature) in 0.1 M sodium cacodylate buffer, then fixed in 2% w/v osmium tetroxide +
1005 1.5% w/v potassium ferricyanide in sodium cacodylate for 1 h at room temperature. The
1006 biosamples were then rinsed in dd-water, then *en bloc* stained with 1% uranyl acetate in dd-
1007 water overnight at 4 °C. These were then rinsed in dd-water and incubated in freshly made lead
1008 aspartate for 30 min at 60 °C. After another dd-water rinse, the biosamples were dehydrated for
1009 10 min each in 35%, 50%, 70%, 95%, three times in 100% ethanol, and finally in three times in
1010 100% propylene oxide. The dehydrated tissues were infiltrated with Polybed 812 resin (hard
1011 formulation) in resin: PO ratios of 1:3 (1 h), 1:1 (overnight), 3:1 (5 h) and finally 100% resin
1012 overnight. These were transferred to beam capsules and the resin was cured at 60 °C for 48 h to
1013 yield samples ready for vEM. Liver samples were sectioned and stained with Toluidine Blue to
1014 identify periportal and pericentral regions in the tissue. The remaining sample was trimmed and
1015 mounted on an SEM stub, and after a thin coat (approximately 8 nm) of carbon was sputtered,
1016 the specimens were into a FIB-SEM (Zeiss crossbeam 550). The same areas were located using
1017 SEM imaging, and Fields of View (FOVs) for vEM imaging were defined. Once the target cell was
1018 identified, the Fibics Atlas 3D FIB sample preparation workflow was initiated. A 1um thick
1019 protective platinum pad was deposited over the sample using a FIB current of 1.5 nA, after which
1020 tracking and autofocus lines were milled into the platinum surface and subsequently covered by a
1021 FIB mediated deposition of 1 um carbon at 1.5 nA. A coarse trench was milled using a 30nA FIB
1022 beam and fine polished using a 3nA beam. Milling and imaging parameters during the

1023 “continuous mill-and-image” acquisition run were set at 30kV accelerating voltage, 1.5nA FIB
1024 current, and 1.5kV accelerating voltage, 1.1nA SEM beam current. A pixel resolution of 5 nm with
1025 a 10 nm slice thickness was set, with total dwell time of 3.0 us/pixel, and the EsB detector grid
1026 voltage was set at 825 V. Image frame time was approximately 42 s, FIB advance rate was
1027 approximately 13.2 nm/min. The raw image stacks were then registered, inverted and binned
1028 using in-house scripts [52].
1029
1030 **Mitochondria segmentation and image analysis**
1031 Volume EM 3D reconstructions were imported into napari (https://napari.org), and mitochondria
1032 were segmented using the empanada plugin
1033 (https://empanada.readthedocs.io/en/latest/empanada-napari.html) by deploying the deep
1034 learning model MitoNet-mini with standard presets and ortho-inference[53]. The model produced
1035 high-quality mitochondrial segmentations, with some split and merge errors as expected for
1036 crowded mitochondria. These errors were manually corrected using empanada to produce
1037 instance segmentations of mitochondria from PP and PC volumes. Mitochondria that were
1038 partially cut off by the image limits were computationally removed to prevent artifactual
1039 measurements. The surface area, volume, and sphericity of remaining mitochondria (PP: n=175,
1040 PC: n=250) were measured for each instance using in-house scripts based on the scikit-image
1041 library (https://scikit-image.org/).
1042
1043
1044
1045

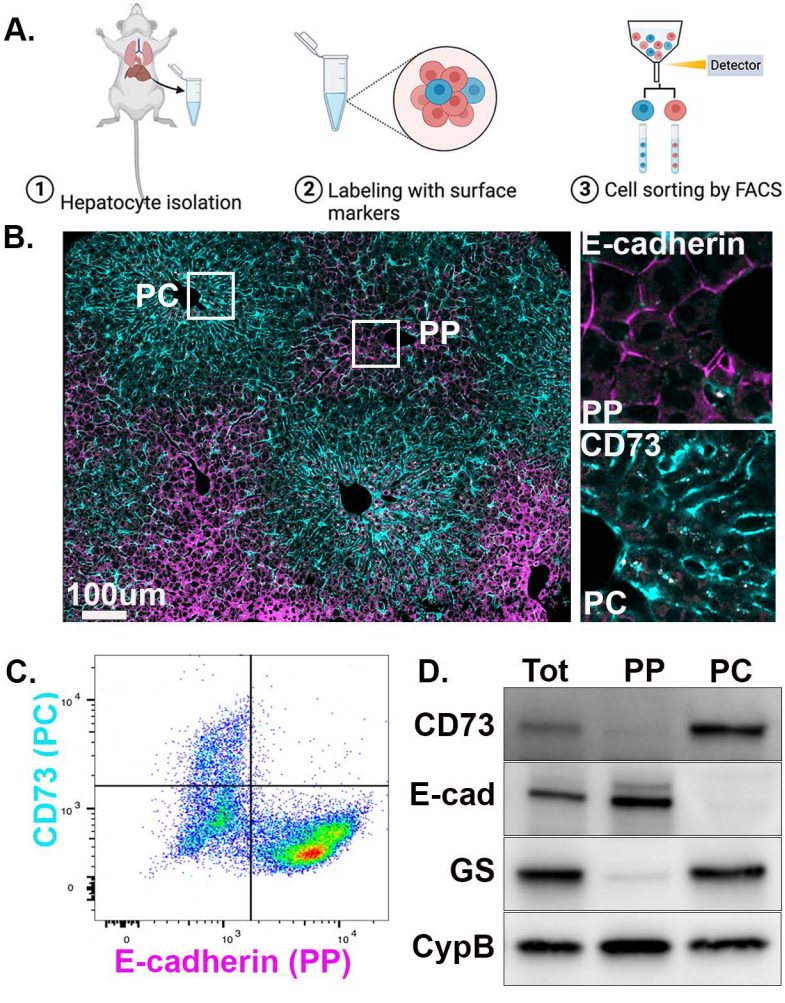

Fig 1. Spatial enrichment of PP and PC hepatocytes

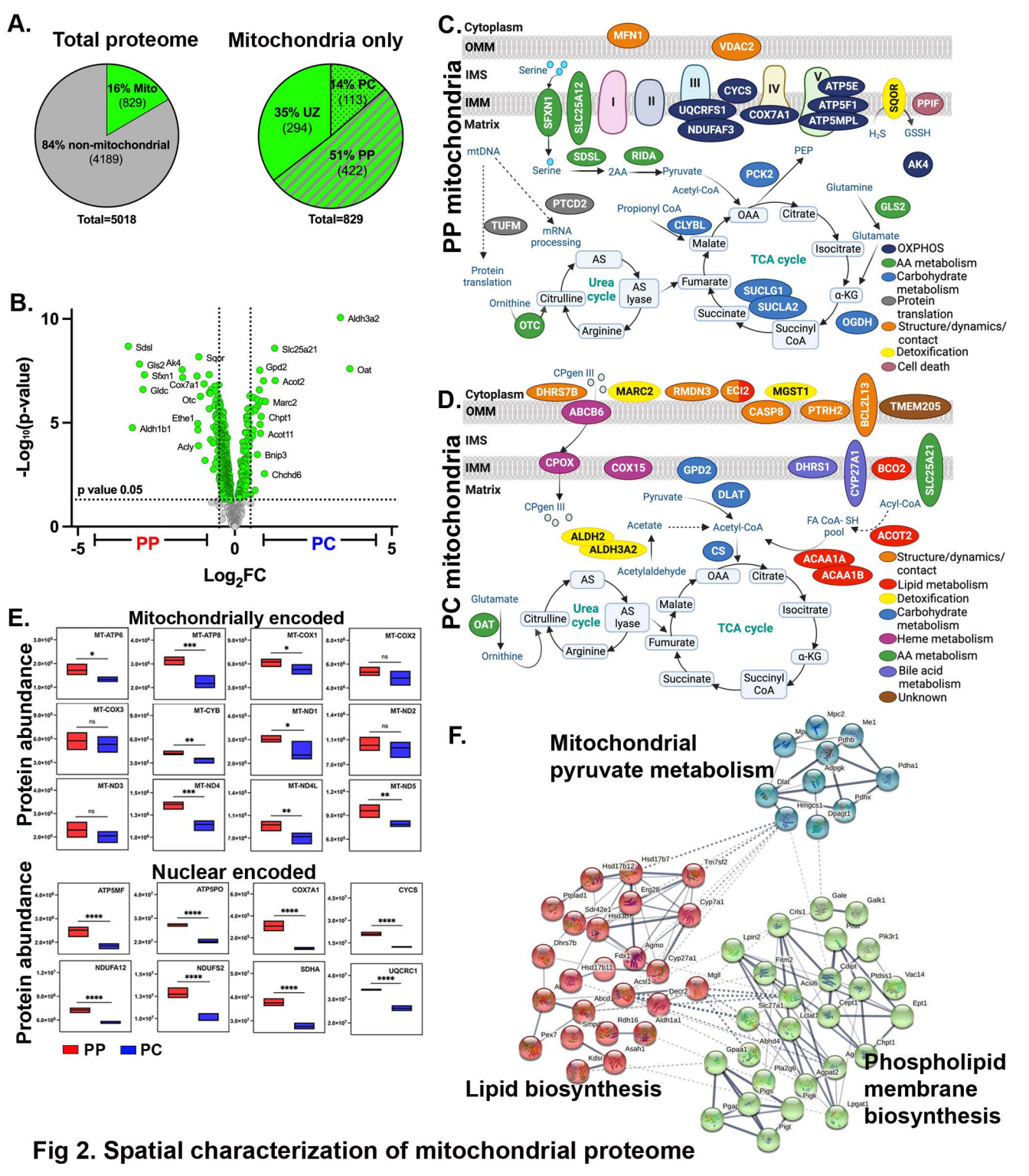

Fig 2. Spatial characterization of mitochondrial proteome

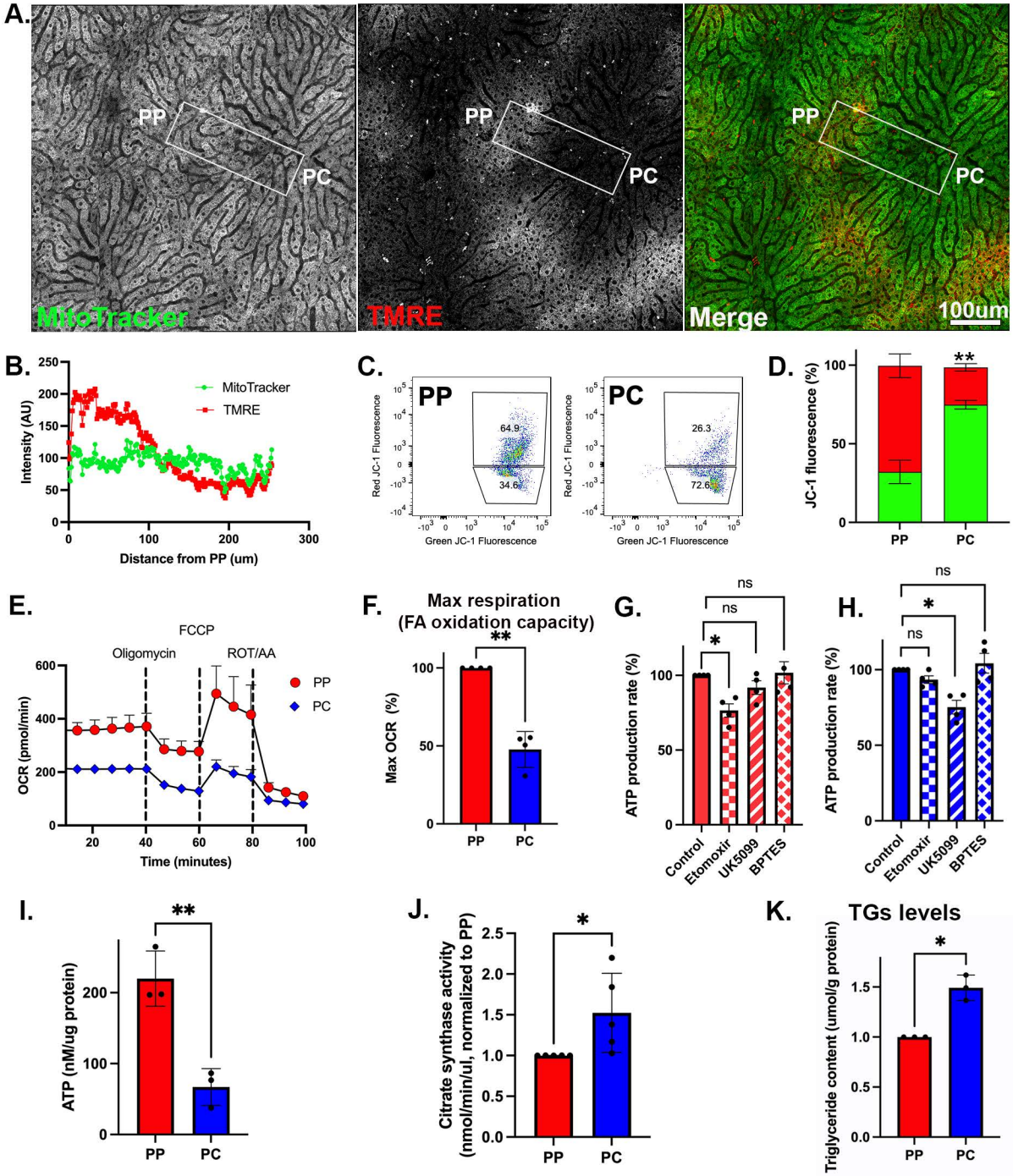

Fig 3. PP mitochondria display higher bioenergetic capacity

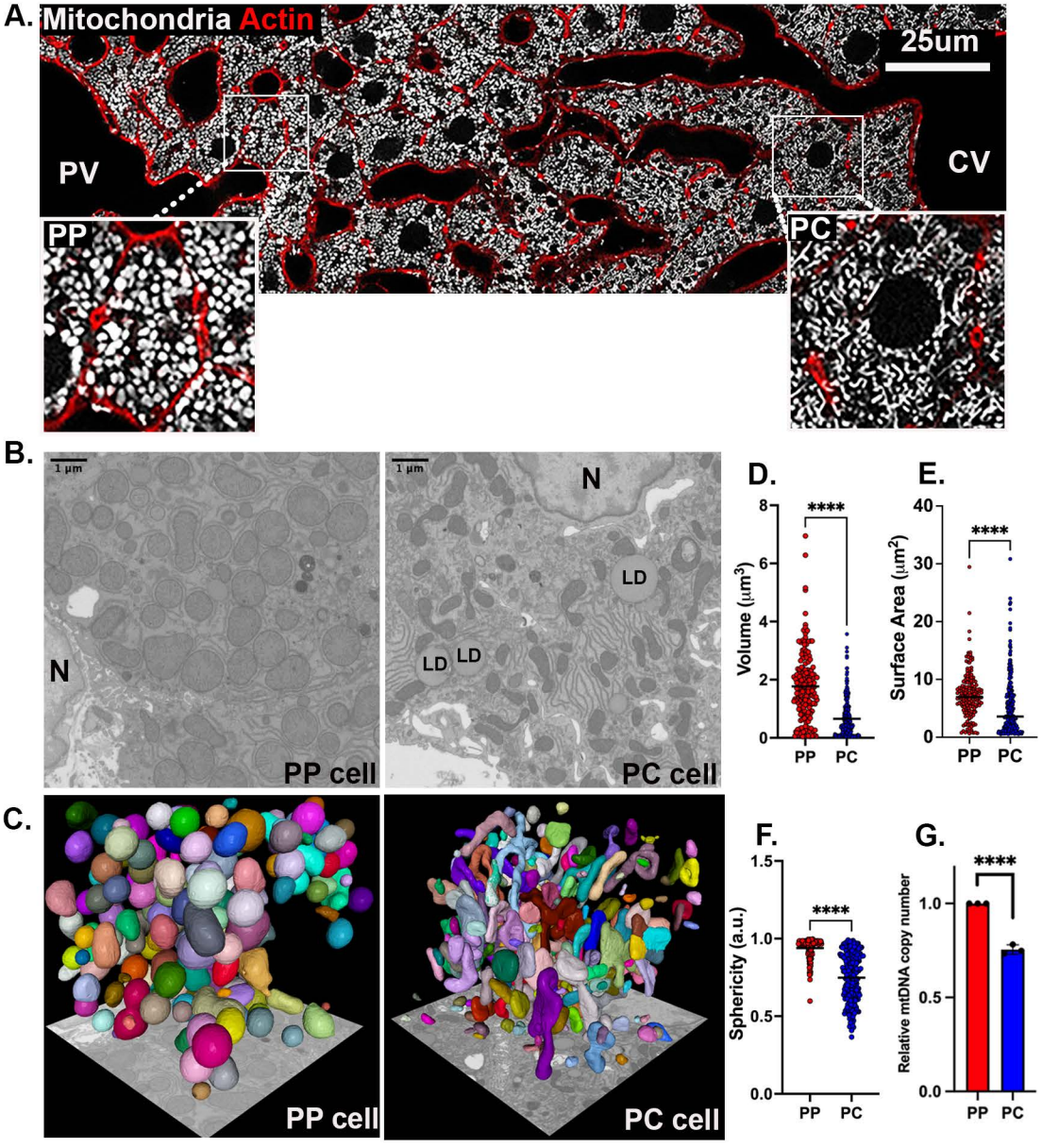

Fig 4. Mitochondrial morphology and organization across the lobule

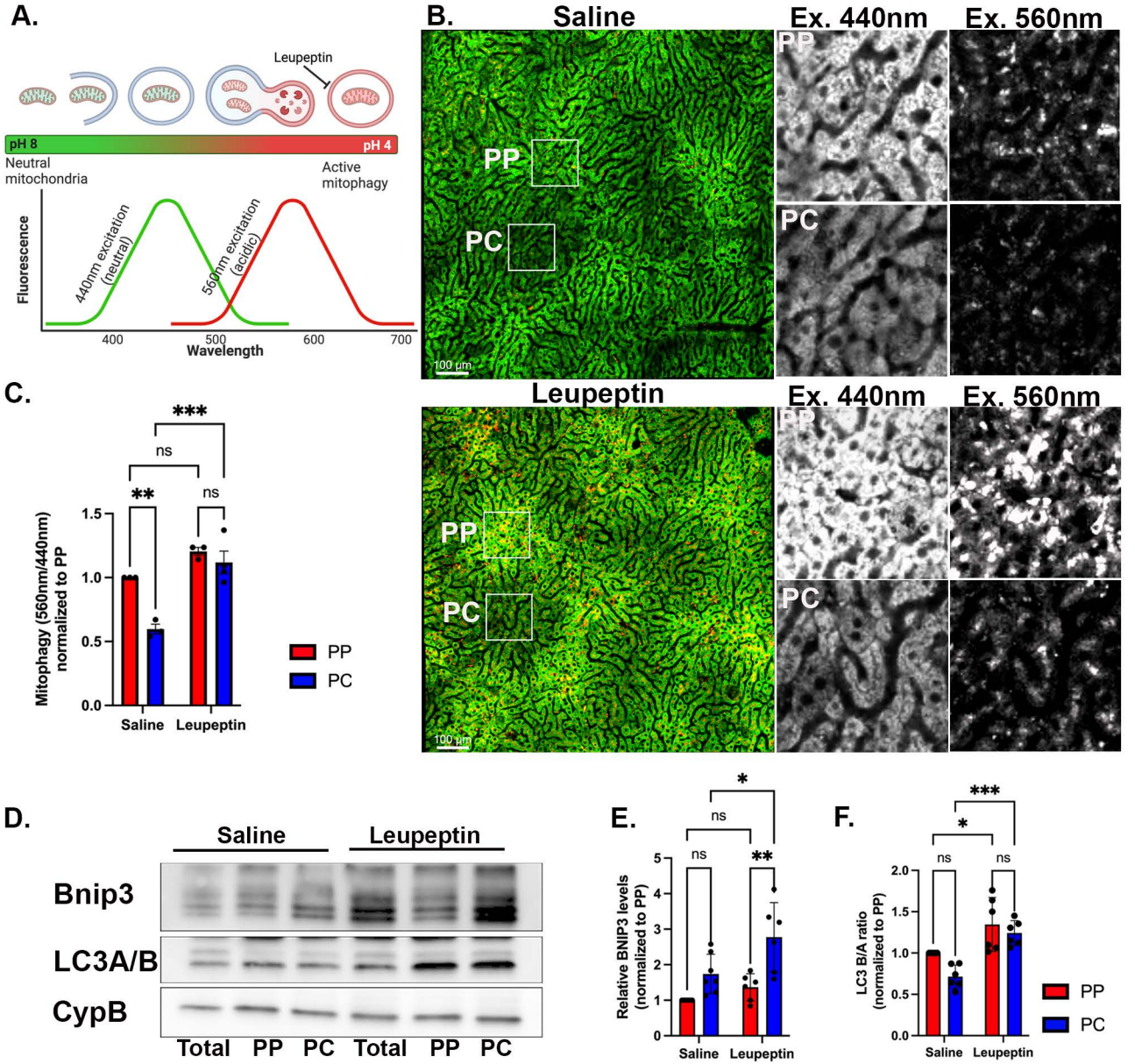

Fig 5. PC hepatocytes display a higher mitophagy flux

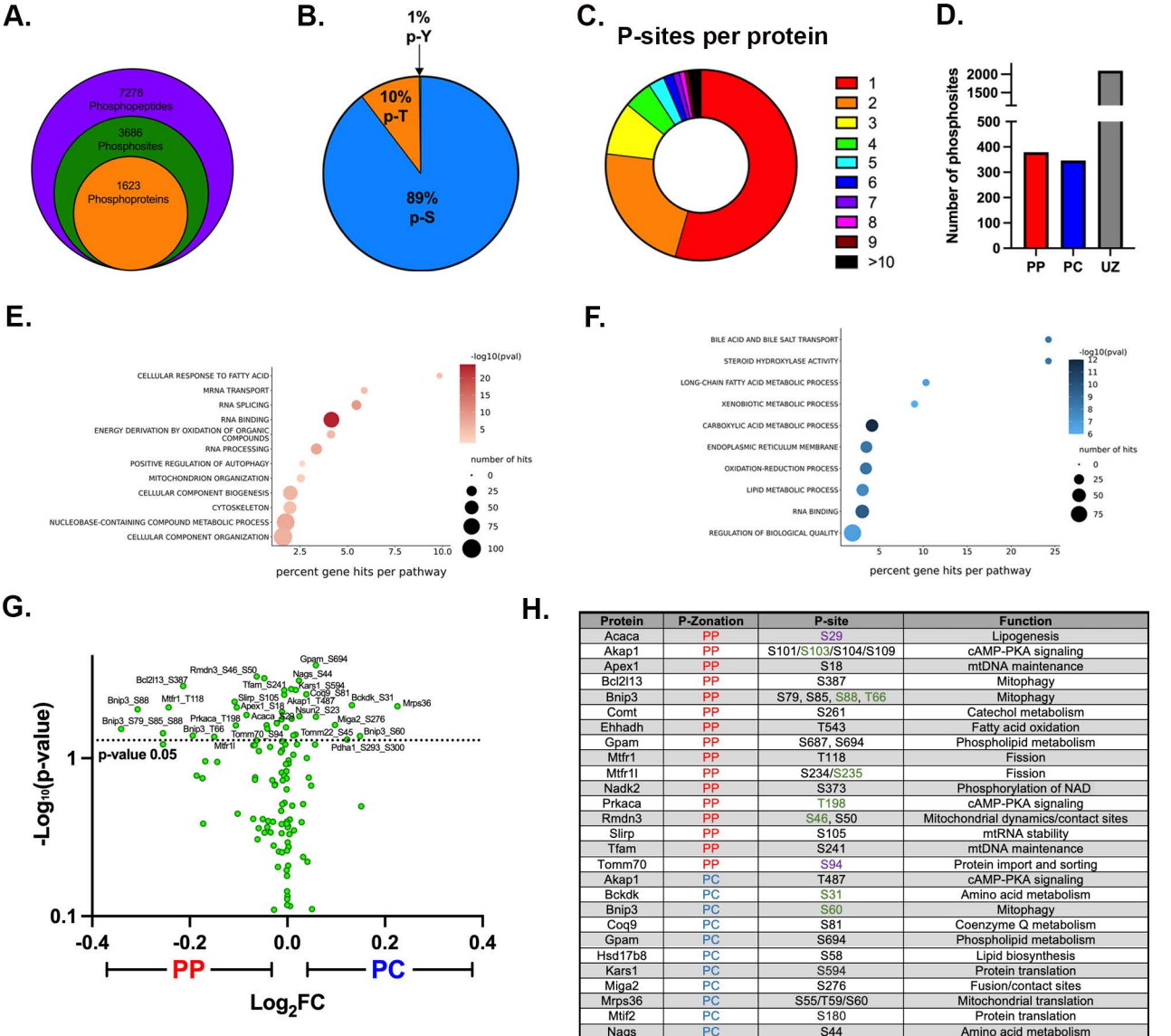

H.

Protein	P-Zonation	P-site	Function
Acaca	PP	S29	Lipogenesis
Akap1	PP	S101/S103/S104/S109	cAMP-PKA signaling
Apex1	PP	S18	mtDNA maintenance
Bcl2l13	PP	S387	Mitophagy
Bnip3	PP	S79, S85, S88, T66	Mitophagy
Comt	PP	S261	Catechol metabolism
Ehhadh	PP	T543	Fatty acid oxidation
Gpam	PP	S687, S694	Phospholipid metabolism
Mtfr1	PP	T118	Fission
Mtfr1l	PP	S234/S235	Fission
Nadk2	PP	S373	Phosphorylation of NAD
Prkaca	PP	T198	cAMP-PKA signaling
Rmdn3	PP	S46, S50	Mitochondrial dynamics/contact sites
Slirp	PP	S105	mtRNA stability
Tfam	PP	S241	mtDNA maintenance
Tomm70	PP	S94	Protein import and sorting
Akap1	PC	T487	cAMP-PKA signaling
Bckdk	PC	S31	Amino acid metabolism
Bnip3	PC	S60	Mitophagy
Coq9	PC	S81	Coenzyme Q metabolism
Gpam	PC	S694	Phospholipid metabolism
Hsd17b8	PC	S58	Lipid biosynthesis
Kars1	PC	S594	Protein translation
Miga2	PC	S276	Fusion/contact sites
Mrps36	PC	S55/T59/S60	Mitochondrial translation
Mtif2	PC	S180	Protein translation
Nags	PC	S44	Amino acid metabolism
Nsun2	PC	S23	RNA modification
Pdha1	PC	S293, S300	Pyruvate metabolism
Tomm22	PC	S45	Protein import and sorting

Fig 6. Phosphoproteome highlights spatially regulated pathways contributing to mitochondrial phenotypes

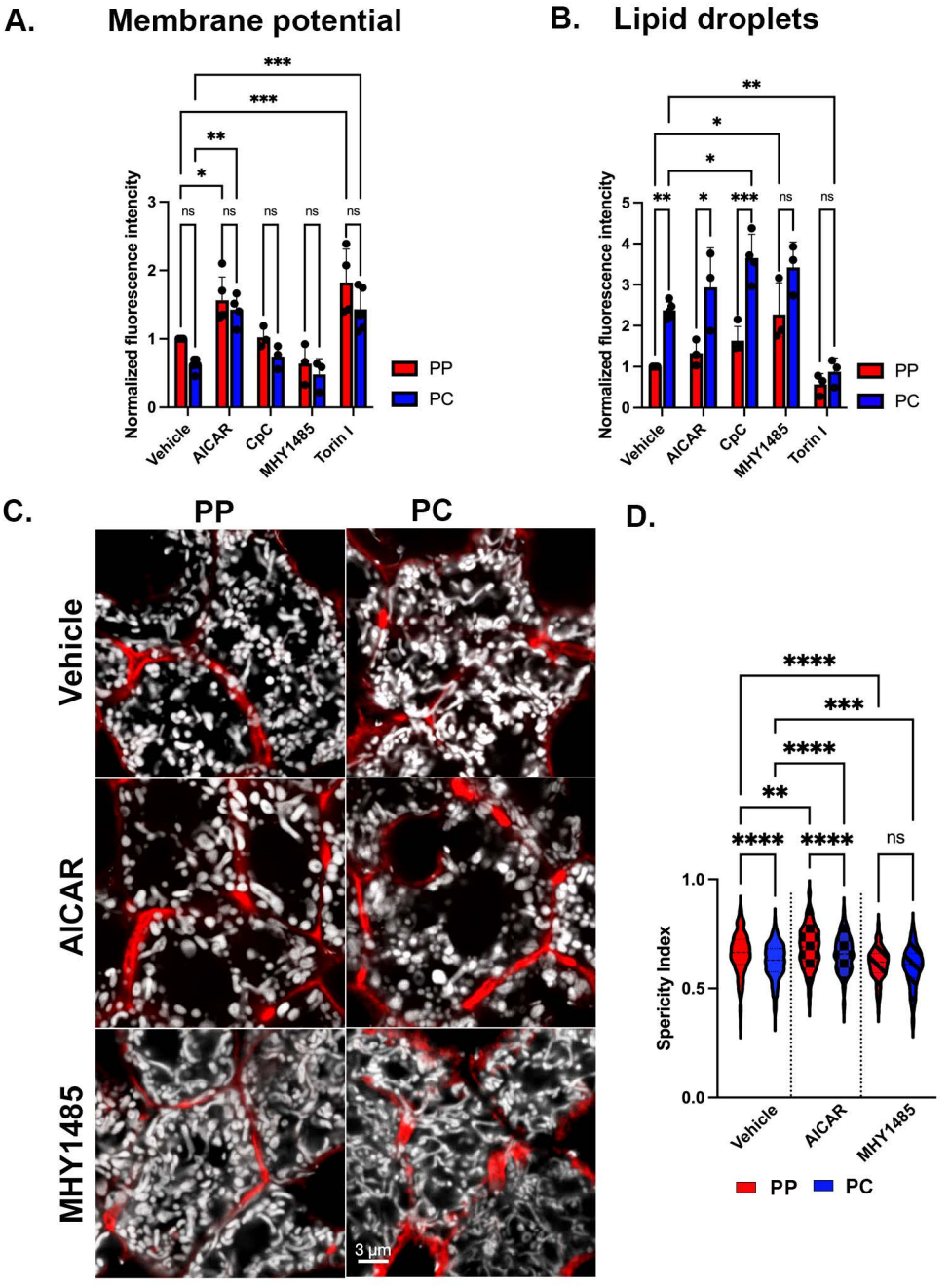

Fig 7. Nutrient sensing signaling contribute to mitochondrial functional and morphological diversity

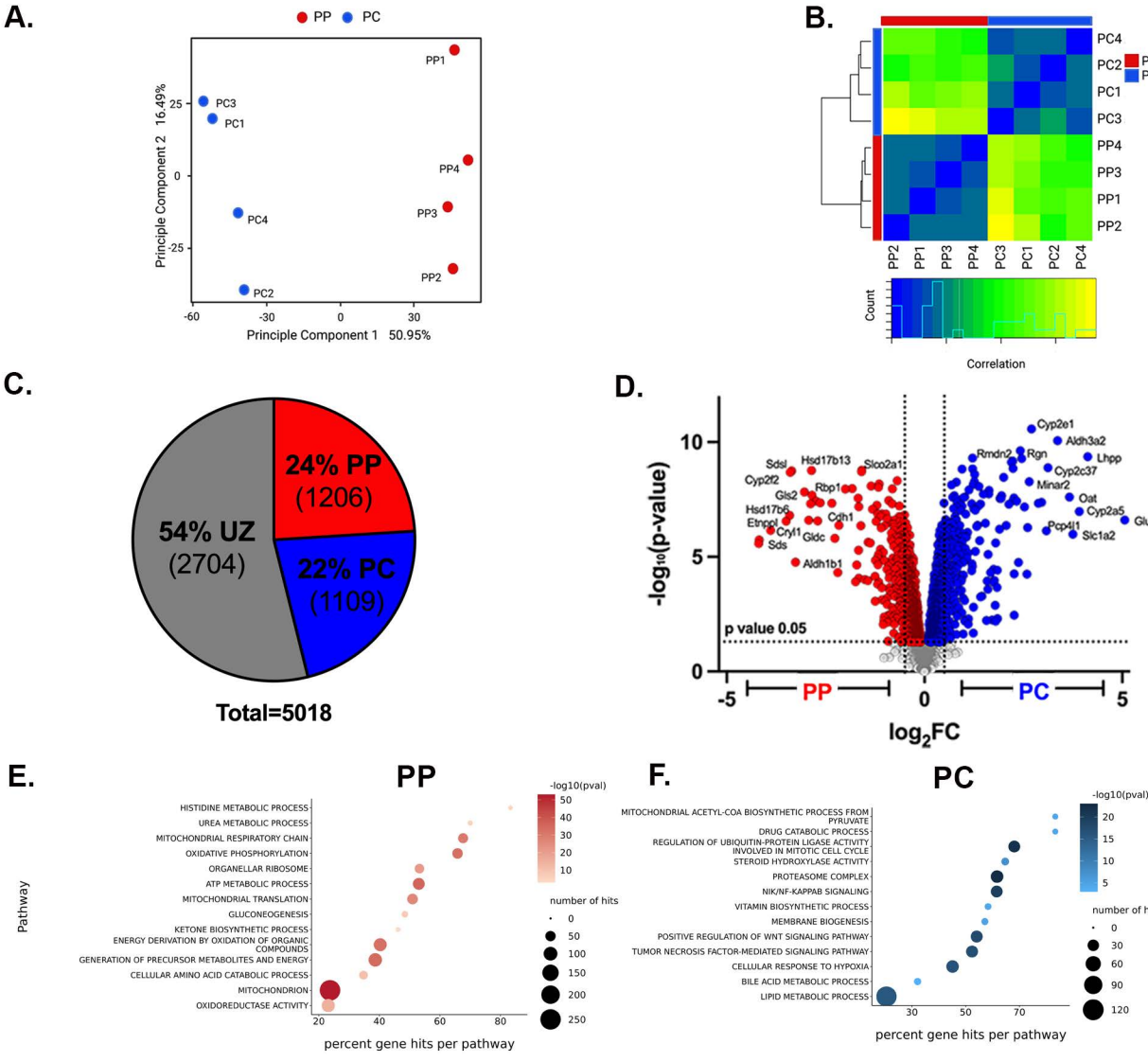

Fig S1 Comparative proteomics of spatially sorted hepatocytes

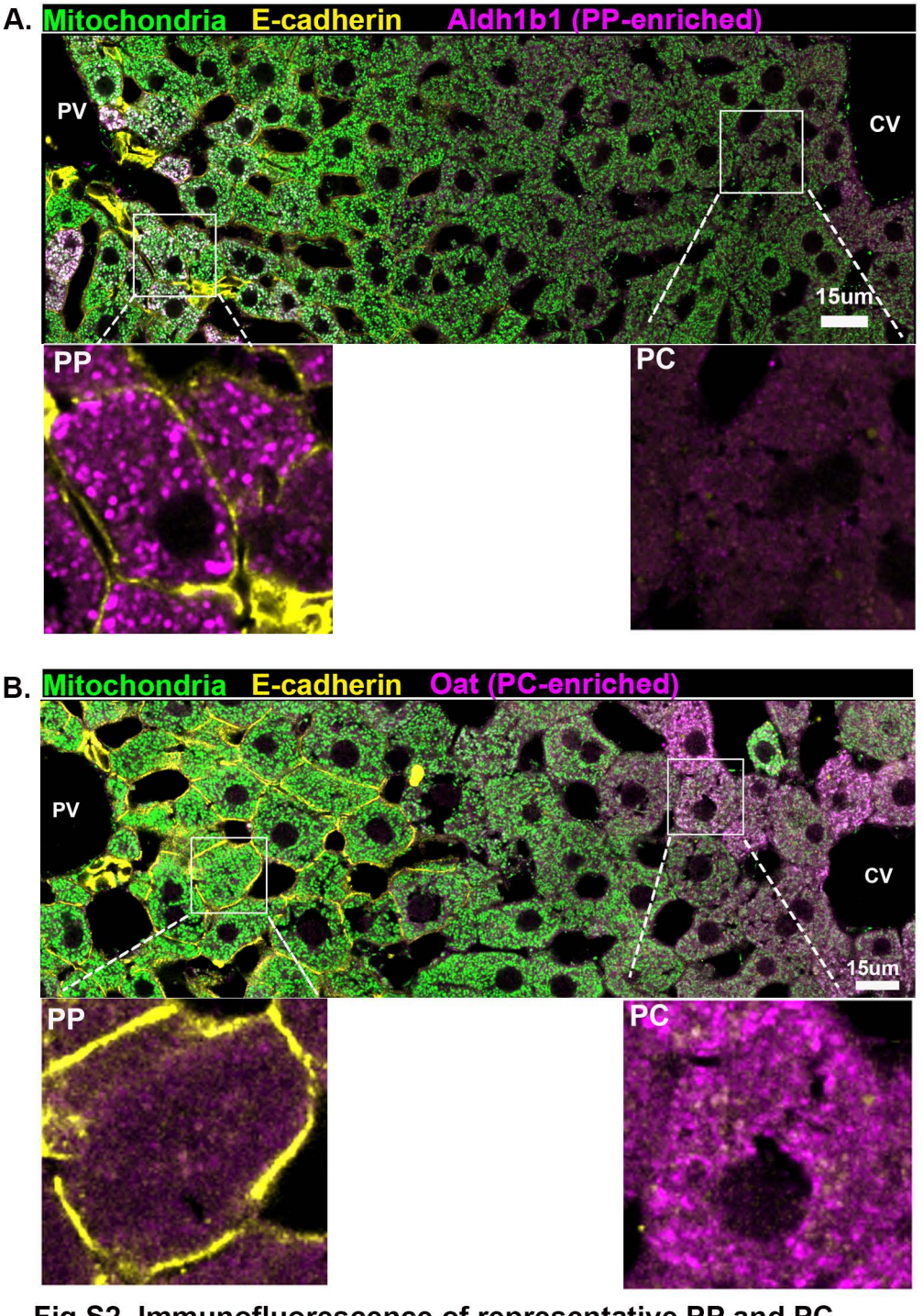

Fig S2. Immunofluorescence of representative PP and PC mitochondrial proteins

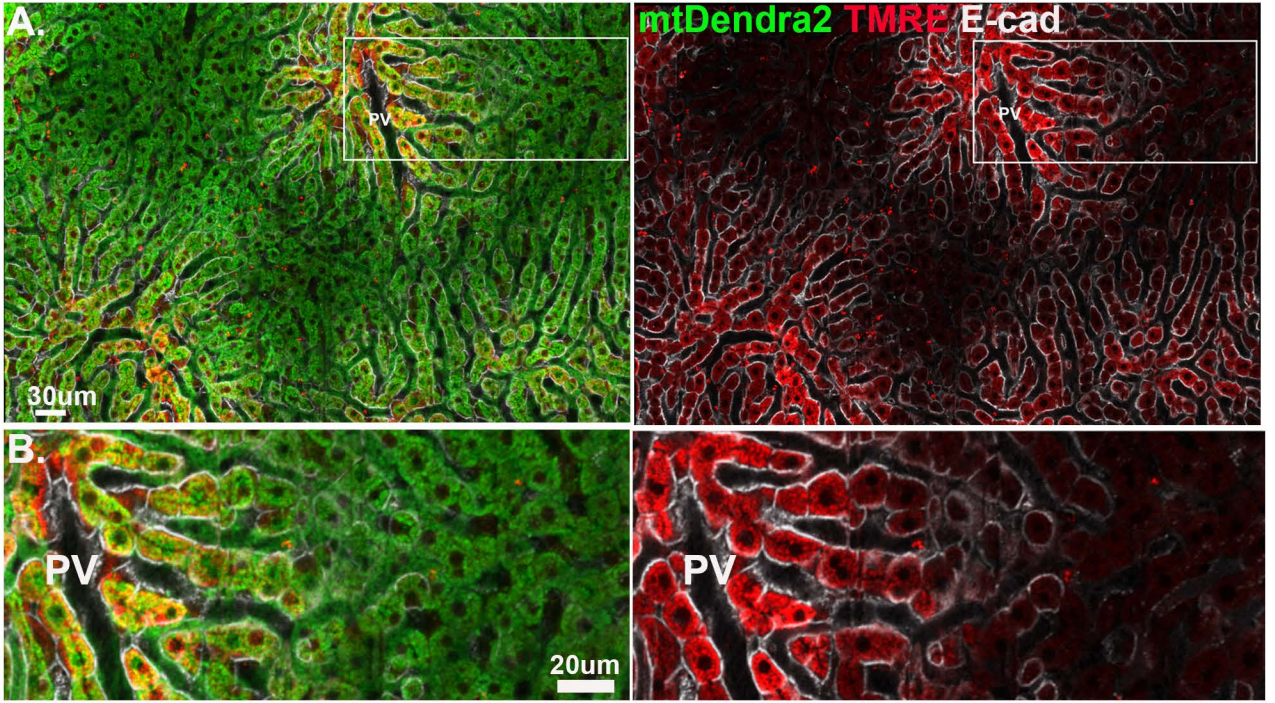

Fig S3. E-cadherin positive hepatocytes display higher membrane potential

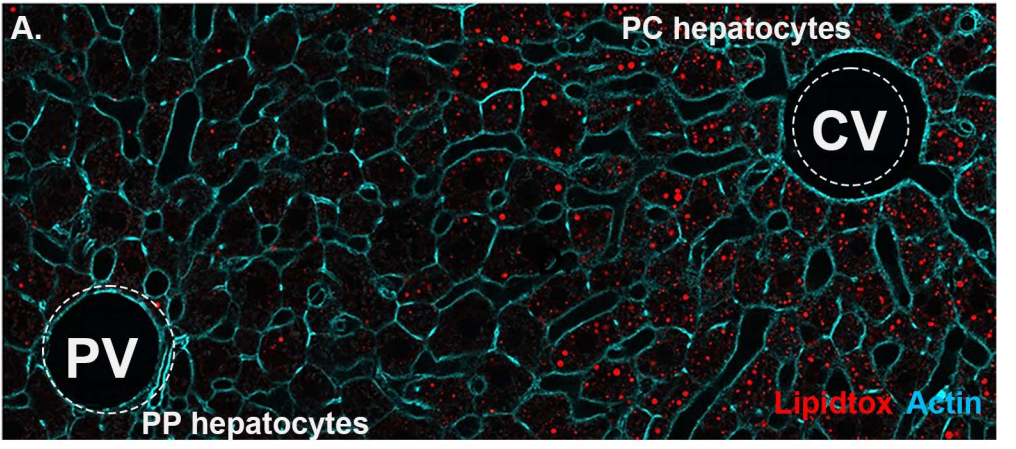

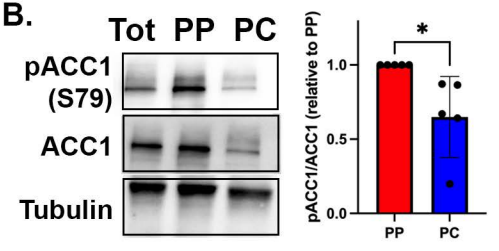

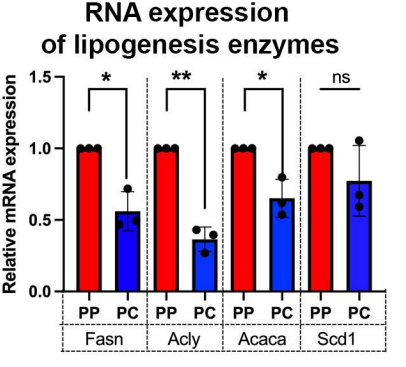

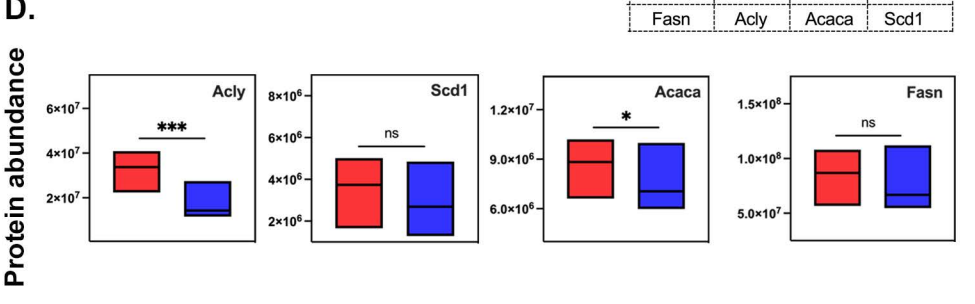

Fig S4. Lipid synthesis is pericentral in the murine liver

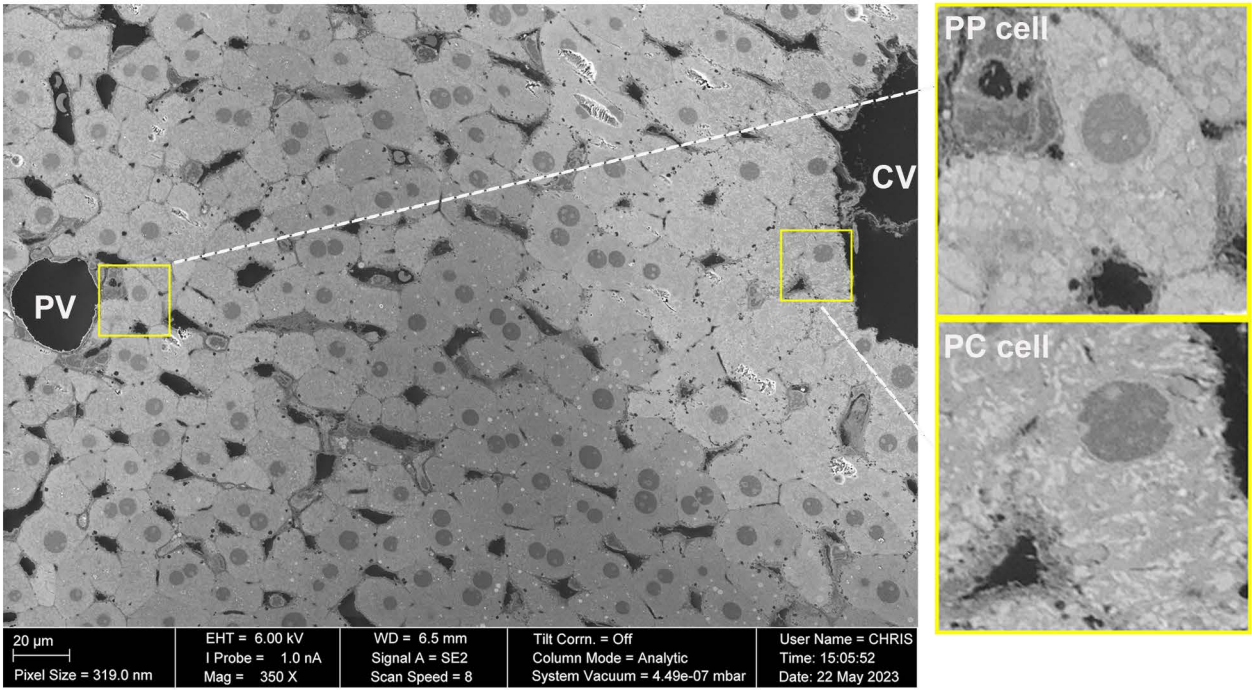

Fig S5. Scanninig Electron Microscopy of the lobule highlighting regions of interest selected for FIB-SEM

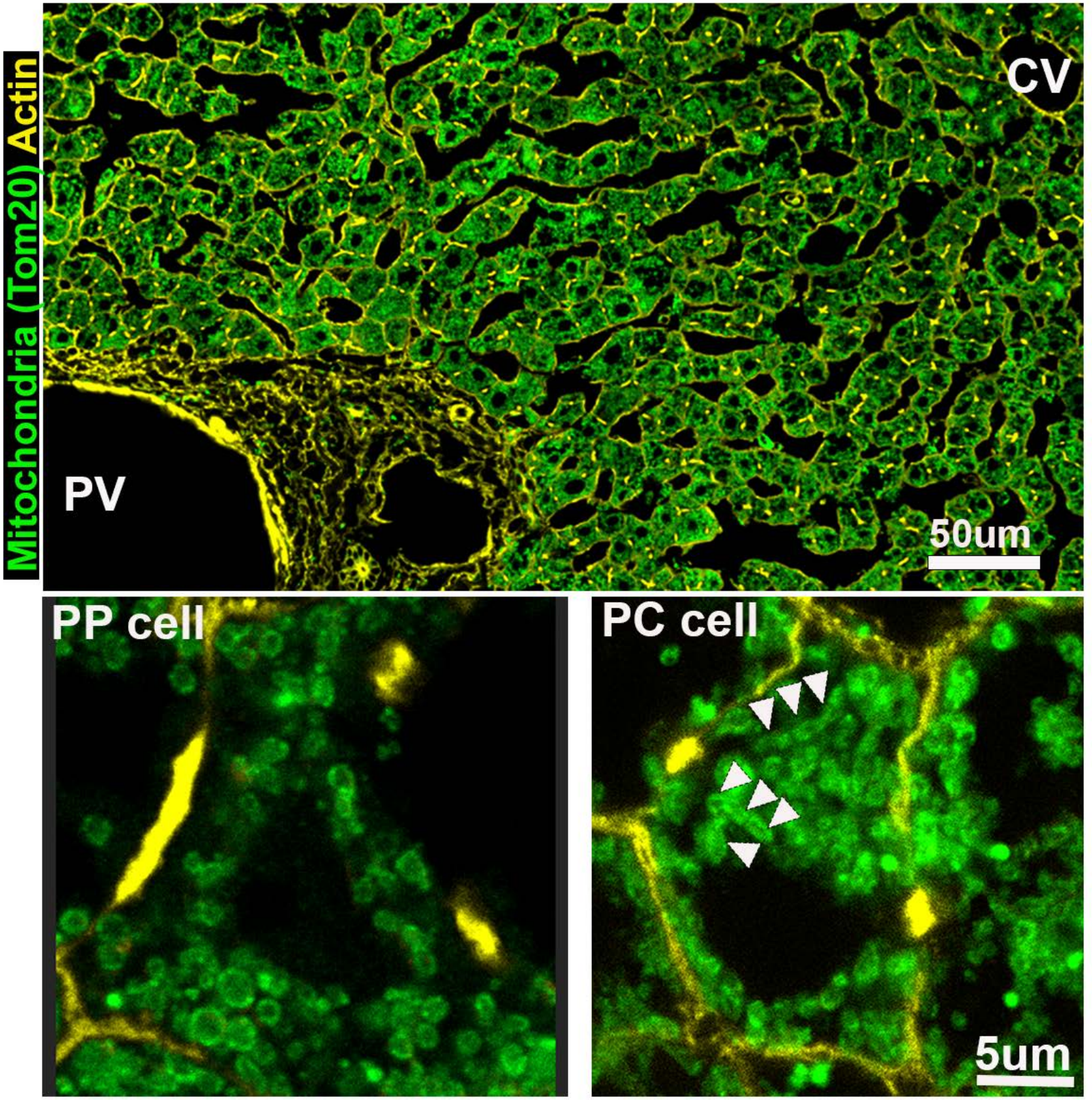

Fig S6. Mitochondrial morphologies are conserved in the human liver

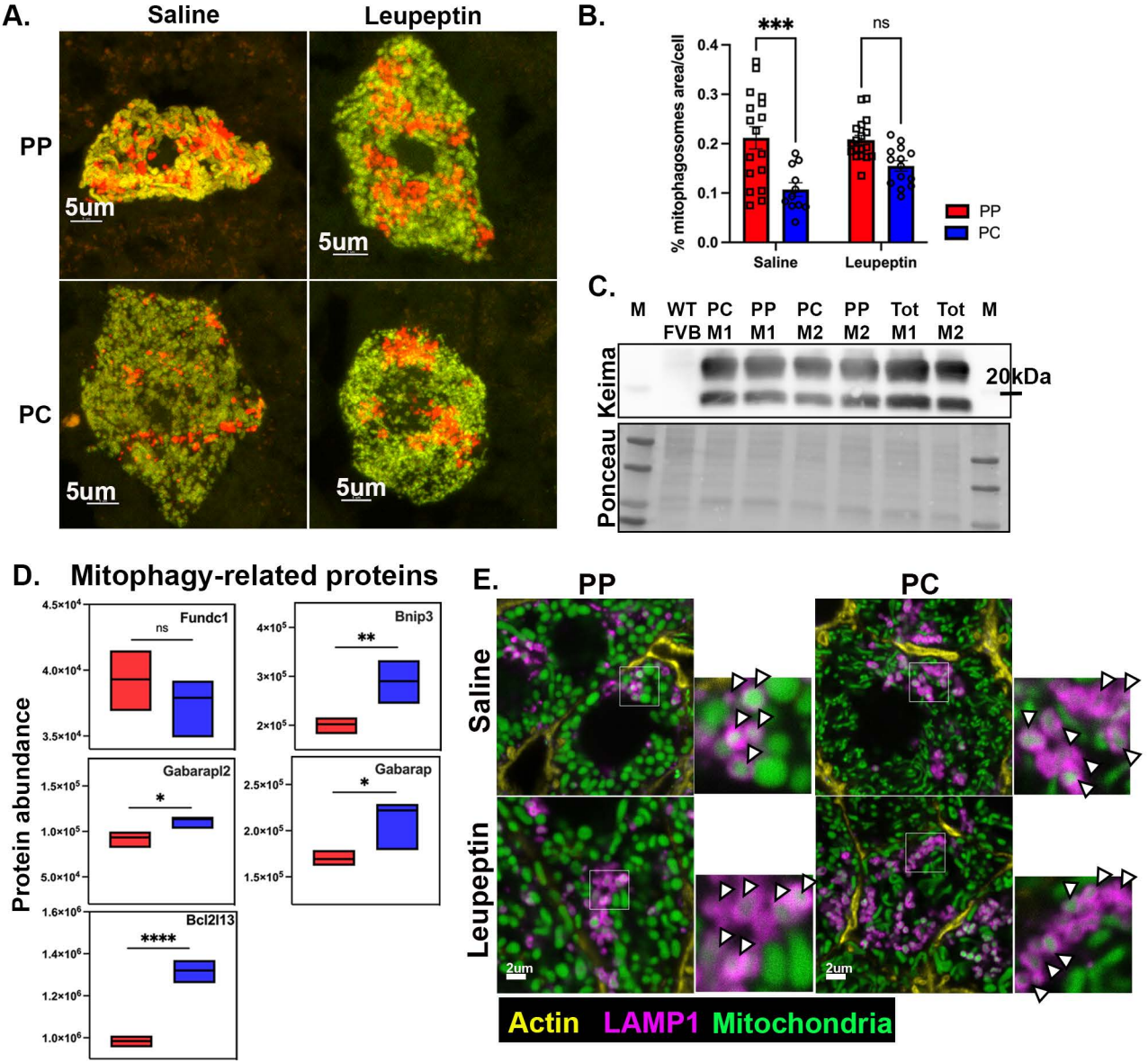

Fig S7. PC hepatocytes display a higher mitophagy flux

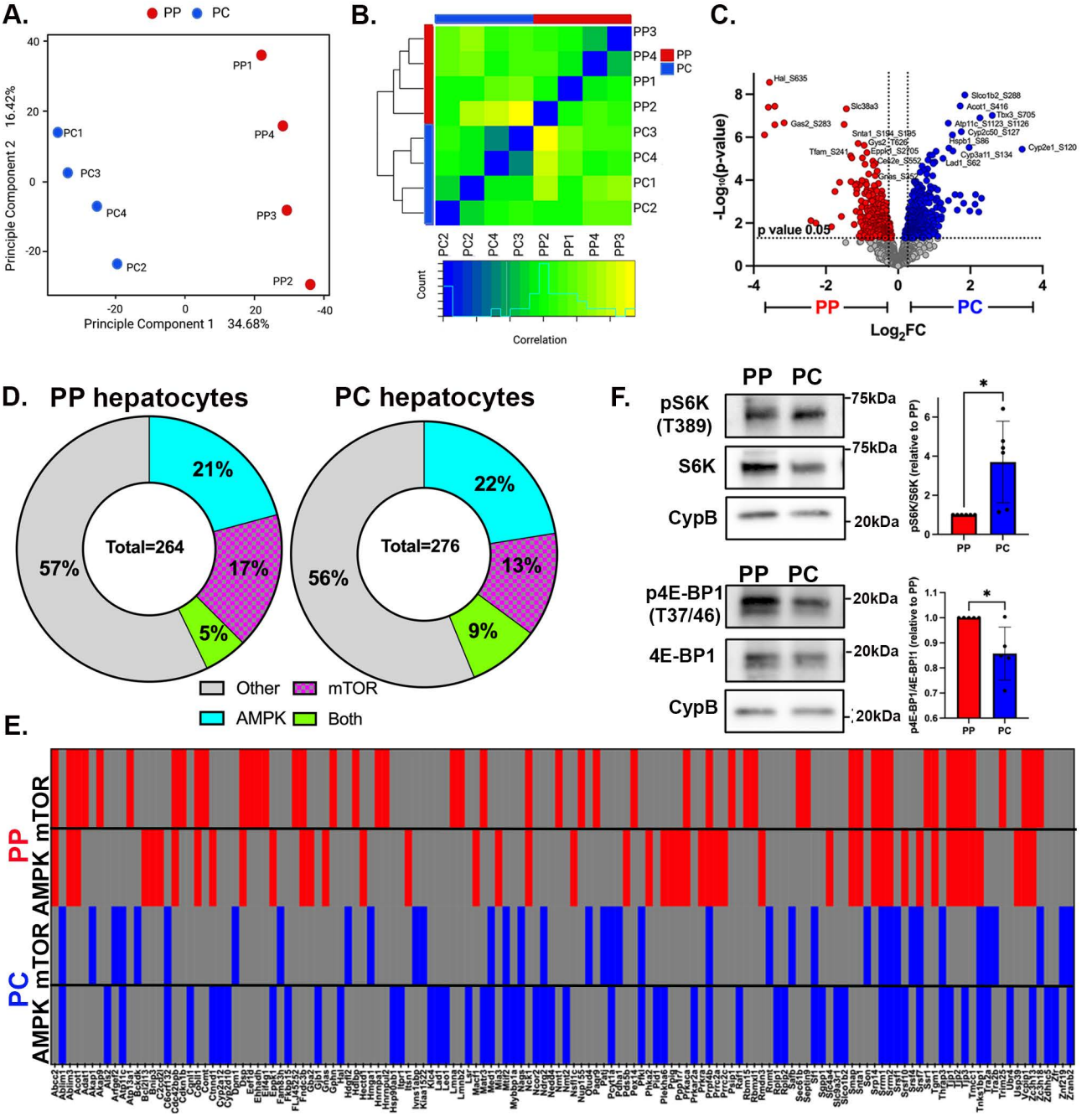

Fig S8 Hepatocyte phosphoproteome

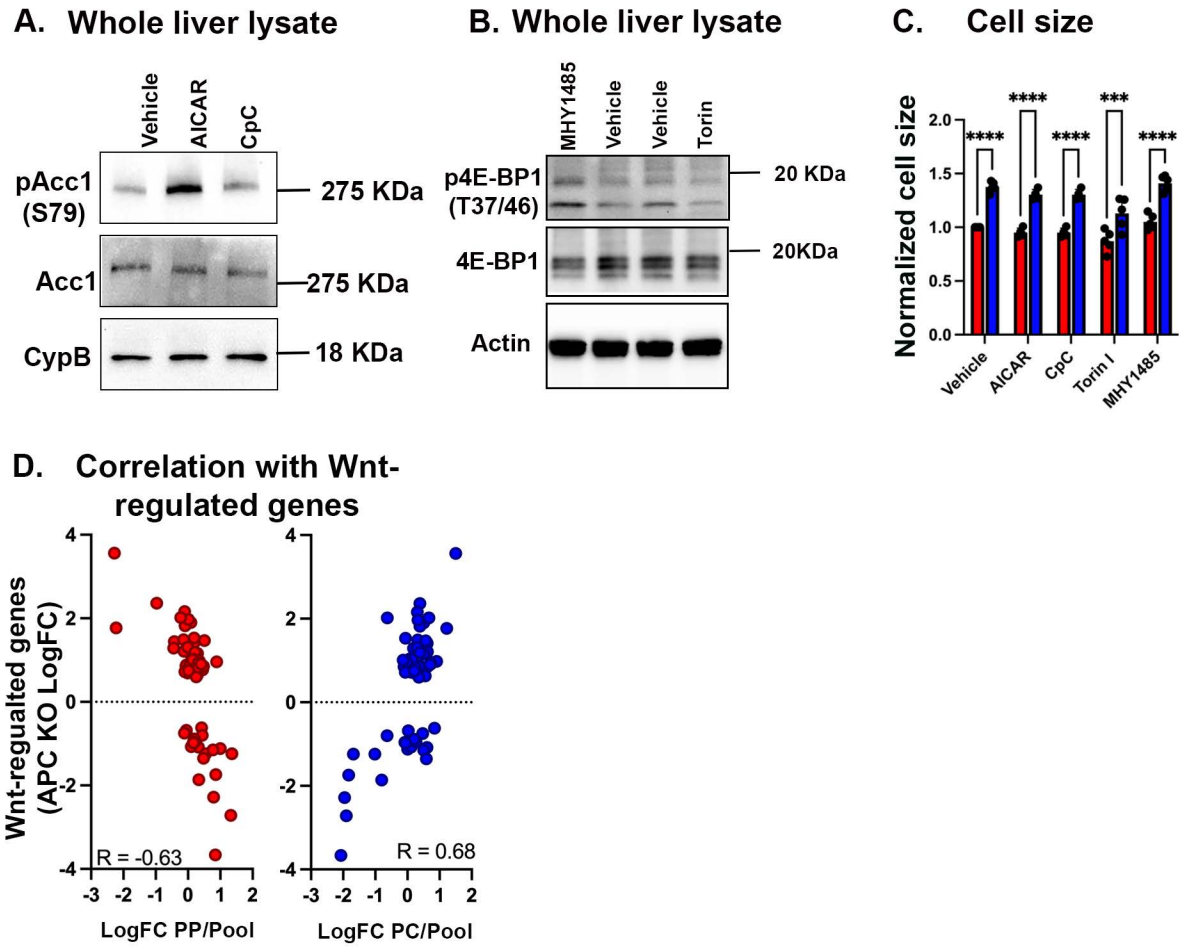

Fig S9. Nutrient sensing signaling regulates mitochondrial heterogeneity